Summer 2020

A Machine Learning System for Glaucoma Detection using Inexpensive Machine Learning

Jon Kilgannon
jk880380@wcupa.edu

A Machine Learning System for Glaucoma Detection using Inexpensive Computation

A Thesis

Presented to the Faculty of the

Department of Computer Science

West Chester University

West Chester, Pennsylvania

In Partial Fulfillment of the Requirements for

the Degree of

Master of Science in Computer Science

By

Jon C. Kilgannon

August 2020

Acknowledgements

I would like to thank my wife, Ivy, for her infinite (and much appreciated) patience throughout my work on this project. Without her support, this would not have been possible.

I would also like to thank my advisor, Dr. Richard Burns, for his equal patience and invaluable advice.

Abstract

This thesis presents a neural network system which segments images of the retina to calculate the cup-to-disc ratio, one of the diagnostic indicators of the presence or continuing development of glaucoma, a disease of the eye which causes blindness. The neural network is designed to run on commodity hardware and to be run with minimal skill required from the user by packaging the software required to run the network into a Singularity image. The RIGA dataset used to train the network provides images of the retina which have been annotated with the location of the optic cup and disc by six ophthalmologists, and six separate models have been trained, one for each ophthalmologist. Previous work with this dataset has combined the annotations into a consensus annotation, or taken all annotations together as a group to create a model, as opposed to creating individual models by annotator. The interannotator disagreements in the data are large and the method implemented in this thesis captures their differences rather than combining them together. The mean error of the pixel label predictions across the six models is 10.8%; the precision and recall for the predictions of the cup-to-disc ratio across the six models are 0.920 and 0.946, respectively.

Table of Contents

List of Tables

List of Figures

1: Introduction

1.1. Overview

Glaucoma is a disease which causes vision loss due to “damage to the optic nerve head” (Foster 2002). It is the “second most common cause of blindness and the most common cause of irreversible blindness worldwide” (Budenz 2013). While the ultimate causes of glaucoma are not certain, the disease can be detected and its progression can be tracked, among other factors, by ongoing loss of vision in the patient’s visual field and by observable damage to a portion of the retina in the rear of the eye called the optic disc (Martus 2005; Tsai 2003).

The focus of this thesis is the detection of changes in structures in the back of the human eye which can be indicative of the presence of glaucoma. Human specialists can measure these structures using either hand-tools or dedicated imaging machinery, but it requires ophthalmological training to discern the location of the structures and to measure them properly. The system implemented in this thesis, called GlauNet, is a neural network which has been trained to emulate the retina measurements which would be taken by six different ophthalmologists.

Negative changes in the visual field of glaucoma patients are observed in 76% of untreated patients versus 59% of treated patients, so detection and treatment are vital to maintaining vision (Forchheimer 2011). In the later stages of the disease, the changes to the eye caused by the progression of glaucoma are permanent and cannot be corrected by medical intervention (Kessing 2007). Measurement solely of intraocular pressure, a standard measure for the risk of glaucoma, can fail to detect asymptomatic glaucoma in the earlier stages of the disease, so it is a net positive if other methods of testing can be used as well (Kessing 2007; Tsai 2005).

A method of detecting glaucoma without requiring the presence of a trained medical professional is vital to discover potential patients in vulnerable or underserved populations. In a study of 5,603 adult, urban West Africans performed between 2006 and 2008, 6.8% of those tested were diagnosed with glaucoma, and 2.5% were already blind. Only 3.3% of those who had been tested had known they had glaucoma before the diagnosis (Budenz 2013). Primary open-angle glaucoma is six times more common among African Americans than among white Americans, and the onset of the disease is a decade earlier. Ophthalmological services are underutilized even in American urban settings, where health professionals can be found within close proximity to a prospective patient (Sommer 1991).

An inexpensive method which detects the risk of glaucoma, and which also requires little or no training, would significantly increase the opportunity for persons in underserved communities to have potential glaucoma detected and treated. Therefore, one primary design factor is for GlauNet to run in a timely manner on inexpensive hardware with minimal software installation required, so all the software which is required to run the network has been packaged in a container which runs under Singularity, an open-source operating system virtualization program. Further, the use of mechanical methods of measurement will create uniformity between measurements, which allows for more precise tracking of the change in measurements of the eye over time and will thereby lead to better outcomes (Fanelli 2013).

If a disease "has a long preclinical phase with insidious onset, symptomless progression," and has many methods of useful treatment, then it is an excellent candidate for frequent and widespread screening. Glaucoma meets these conditions for screening desirability (Mohammadi 2013), and if a method of screening can be automated, this would make it possible to make screening more common.

1.2. Glaucoma Detection via the Cup-to-Disc Ratio

The optic nerve carries signals from the retina to the brain. The portion of the head of the optic nerve which can be observed on the surface of the retina is called the optic disc. The portion of the retina containing the optic disc can be captured by a fundus camera to form a fundus image. The optic disc "contains a central depression" called the physiologic cup or optic cup, which is visible on a fundus image as an oval spot, interior to the optic disc, which is lighter in color than the main body of the disc. Atrophy of the optic nerve can be observed on the surface of the retina in the form of changes to the shape and relative sizes of the optic cup and disc, the latter of which can be detected by measurement of the ratio of the area of the cup to the area of the disc (hereafter the *cup-to-disc ratio* or *C/D ratio*) (Tsai 2003; Foster 2002).

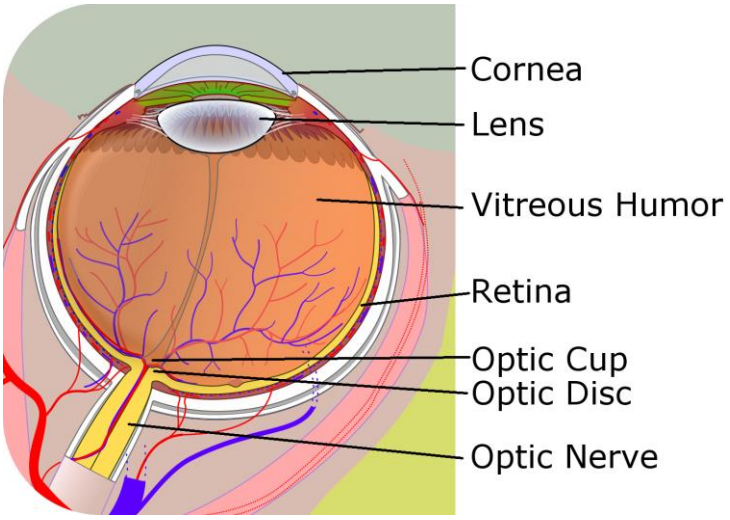

Figure 1: Features of the human eye important to this project
Unannotated image by Jordi March i Nogué, made available under Creative Commons v 3.0

The cup-to-disc ratio was proposed in 1967 as a diagnostic tool for evaluation of the optic nerve and for communicating its properties (Armaly 1967; Danesh-Meyer 2006). A number of studies since its proposal have found that the cup-to-disc ratio is among the best predictive performers among measures of the risk of glaucoma, with an area under the ROC curve of "close to 0.90," where 1.0 means that a model's predictions are 100% correct (Edward, 2013; Google

2020). The cup-to-disc ratio is among the morphometric variables of the eye which can be used to diagnose glaucoma, together with the condition of the sectors of the rim area around the optic cup and parapapillary atrophy (defined as "abnormalities in...the region adjacent to the optic disc border") (Martus 2005; Wang 2013). Morphometric variables – the shape of formations within the eye – are often tractable to machine learning procedures.

1.3. Outline

This thesis proceeds as follows:

- In Section 2, an overview of related work is presented. The human-mediated methods of detecting glaucoma are briefly examined, then previous work in detecting glaucoma with machine learning is considered. Other work which has used the same data set as this thesis is also noted. Finally, other inexpensive medical computing systems are briefly discussed.
- The image data that are used in this project are presented in Section 3. The data itself are presented, with discussion of the methods that were used by the creators of the data corpus in annotating the images. The methods used to capture the annotations from the data corpus's images are described.
- The architecture of the neural network is described in Section 4. A brief primer of neural networks is given. U-Net, the specific architecture used in this project, is explained. Then a severe imbalance among the classes in the annotations is presented, the reason why this imbalance is an issue for the network is discussed, and the method used to ameliorate the imbalance is described. Lastly, the process of deciding what values to use for the network's hyperparameters is given.

- Data on the performance of the neural networks are presented in Section 5. The process of training the networks and their correctness are described.
- Section 6 describes the design of the Singularity container used to make the system easier for the user to install and use, and then presents the time required to run the six networks in Singularity on a cloud instance which duplicates the specifications of inexpensive hardware.
- The conclusion in Section 7 describes further work which is possible with this project, and briefly sums up the system's correctness.

2. Related Work

2.1. Overview

A number of machine learning techniques for calculating the cup-to-disc ratio (C/D ratio) exist; the primary ones focus on either segmentation of a fundus image, or segmentation of an image captured by Optical Coherence Tomography (OCT), a more complex technology which captures slices of the retina. The GlauNet project considers fundus images. In machine learning projects, both fundus and OCT images are segmented either by numerical analysis of the pixels in the image, or by neural networks analyzing the image in a more complex manner.

This section considers other projects which use the RIGA dataset used to train this project, and then briefly discusses other projects which utilize or describe inexpensive medical computing.

2.2. Non-Machine Methods of Glaucoma Detection

Until recently, all tests for the detection of glaucoma were – of necessity – performed by humans with specialist training. Some methods of glaucoma detection such as gonioscopy, observation of the point where the cornea and iris meet, have been described as "very much an acquired art" (Kessing 2007). Several other methods of glaucoma detection require training or equipment which is not found in the general population, or have inherent uncertainties due to their methods of operation. Applanation tonometry requires using a small device, after an anesthetic is applied, to flatten part of the cornea. The device must be kept sterile to prevent the transfer of infections, and it must be calibrated on an ongoing basis. Pneumatonometry uses a different small tool, and requires trained skill to read its measurement from a waveform graph. Stereoscopic optic nerve photography requires the operator to outline the optic disc

margin and “center the optic nerve in the image.” The slow scanning speed of Optical Coherence Tomography, which as mentioned above is a popular source of data for machine learning work, leads to “motion-induced artifacts” that can make it imprecise. Digital palpitation requires no equipment, but it requires professional experience as the eye is touched by the ophthalmologist and the pressure is estimated (Edward, 2013). An automated process would be valuable, allowing the creation of diagnostic information without the need for specialist interpretation.

2.3. Related Machine Learning Work

GlauNet captures the cup-to-disc ratio using a U-Net neural network to segment the fundus image, but other methods for determining the ratio are possible. In 2009, Liu et al proposed the ARGALI system to automatically calculate the cup-to-disc ratio from a fundus image. This early system segments the optic disc using eight separate methods. First the disc is segmented using a level set function, a form of numerical analysis, to separate the image by analysis of the red channel of the color space. Then an ellipse is fitted around the irregular region discovered by the level set for half of the disc segmentations. The cup is segmented both by a level set with thresholding, and by considering the color intensity of the pixels. Half of these segmentations have ellipses fitted around them as well. The authors state that segmenting the optic cup is “more challenging than the optic disc segmentation” due to the cup boundary being less visible than the disc boundary. Eight separate combinations of these methods of segmentation are fed into a neural network, which creates a prediction based on the eight segmentations that were fed to it. The predictions made by the neural network are compared with segmentations made by several ophthalmologists, and those predictions which are within a

threshold value of the intra-observer differences are considered to be "within limits" and are therefore considered a successful segmentation of the image. Ninety percent of the segmentations were within limits (Liu 2009).

The mean error for GlauNet's predictions is 10.3%, and the mean correctness of its predictions 89.7% (see Section 5.2.1). However, this thesis does not define a threshold value as Liu did; the correctness definition used in this thesis directly compares the predicted class mask to the ground truth of each individual annotator, and the correctness is the percentage of correctly labeled pixels in a predicted class mask, or is the proper classification of a C/D ratio as a positive or negative diagnosis.

In 2015, Nathiya and Venkatesewaran compared several contemporary methods of segmenting the fundus image to calculate the C/D ratio: Otsu's image thresholding method, removal of the blood vessels from the images followed by region growing, hill climbing to find the seed point for K-means clustering, and fuzzy C-means clustering on the red component of the color space. They found that the Otsu method, with 11.04% performance error, performed worst, while fuzzy C-mean clustering was the best with 9.82% performance error (Nathiya 2015). Nathiya defines the performance error percentage in terms of the Experimental C/D ratio Value (ECV) and the Clinical C/D ratio Value (CCV)[1] as:

$$\text{Performance error (\%)} = 100 \times (\text{ECV} - \text{CCV}) / \text{CCV}$$

[1] ECV, the experimental C/D ratio value, is the value predicted by the model. CCV, the clinical C/D ratio value, is the value captured from the human annotator's annotation.

The C/D ratio predictions made by the six models in GlauNet were compared to the C/D ratios captured from the annotations made by their respective six annotators, and the performance error percentage data has been detailed in Table 1. The mean performance error of GlauNet is higher than the median performance error due to outliers that pull the mean error upward. The full ensemble of GlauNet's models compare roughly well to the methods that Nathiya surveys, coming in slightly above the Otsu method. However, two of GlauNet's models – A and D – perform much better than the others, and in fact perform better than any of the methods which Nathiya's team considered.

Model	Annotator	Mean of Performance Error	Median of Performance Error
A	1	8.82%	7.01%
B	2	11.18%	9.50%
C	3	14.47%	11.28%
D	4	7.47%	5.36%
E	5	13.96%	7.20%
F	6	14.25%	11.27%
All	All	11.89%	8.74%

Table 1: Absolute value of Performance Error for the GlauNet models

Similarly to one of the methods Nathiya looked into, Aquino, et al, propose a method for segmenting the optic disc within a fundus image using Prewett and Otsu edge-detection techniques on the red and green channel of the color space individually. A Circular Hough Transform is used to approximate the edges of the optic disc, and then the system chooses the more successful of the red or green approximations. The authors note that automated segmentation of the optic disc can be made difficult by the presence of organic irregularities such as the obscuration of the disc's rim by blood vessels, or by a small movement of the patient's eye creating blurring of the fundus image which is sufficient to cause problems for automated systems but which human annotators can disregard (Aquino 2010). A Circular Hough Transform

was used in a similar fashion by Yin et al, and displayed an average error in area of 10.8% (Almazroa 2017). GlauNet, in comparison, displays a mean error in area of 10.3% (see section 5.2.1).

2.3.1. Optical Coherence Tomography

A more modern and complex method of detecting the features of the retina than fundus imaging is Optical Coherence Tomography (OCT), a noninvasive technology which captures image slices of the retina and allows viewing of the optic disc and cup roughly perpendicular to the plane of a fundus image and gives a three-dimensional view of the retina (Nathiya 2015, Khalil 2018). Research into automatically detecting glaucoma from an OCT image has been limited by the lack of a standard dataset (Khalil 2018). However, attempts have been made with relatively small OCT image sets. Wu, et al, proposed a method using OCT imaging to segment the retina into cup, disc, and other. The method de-noises the noisy OCT image, finds a curve representing the margin between layers of the retina in a 3D image slice, selects points of maximum curvature on the curve, and defines a ring above those points as the edges of the neural canal opening in the optic cup; the optic disc is similarly defined. The algorithm ran on "a 3.30 GHz…PC with 16 GB memory" and required 103 seconds to run, while GlauNet was tested on a 2.2 GHz single-core cloud instance with 4 GB of memory and required 60 seconds to run. The correctness of Wu's process was measured using the Dice similarity coefficient to be 0.919 ± 0.034 for the measurement of the area of the disc, and 0.928 ± 0.116 for the measurement of the area of the cup (Wu 2015).

The Dice similarity coefficient was measured for predictions made by each model in GlauNet (see Section 5.2.2). The mean Dice similarity across all six models for measuring the

area of the disc was 0.886, and the model which performs the best on this metric, Model E, has a mean Dice similarity of 0.907. As a higher Dice metric is better, GlauNet performs slightly worse than Wu's process. However, Wu's method processes OCT images rather than the fundus images which GlauNet takes as an input, and OCT machines are more expensive than fundus cameras, which goes against the goals of this project of creating an inexpensive system.

A separate method for determining the cup-to-disc ratio from an OCT image was described by Ganesh Babu, et al, in 2012. This method detects vertical and horizontal edges in an OCT image slice via a Haar wavelet transform, then uses this information to find the edge between the retina and vitreous humor, and the edges of the choroid layer in the retina, which together help delineate the edges of the optic cup and disc. The authors state the method is "memory efficient," but do not quantify the memory used (Ganesh Babu 2012).

In 2015, Ganesh Babu et al discussed a method for segmenting a fundus image, noted that thresholding techniques alone are not sufficient to segment the optic cup and disc due to "large [color] intensity variations in the cup region," and also that the methods they used require the blood vessels to be removed from the image of the optic cup region by K-means clustering. Their method, similar to the algorithm of Nathiya and Venkatesewaran referenced above, uses fuzzy C-mean clustering (FCM), but differs from Nathiya's method by choosing a form of FCM which accounts for spatial data to capture information in the relationship between pixels. The optic disc is approximately located by finding the "brightest point in the green (G) plane of the fundus image." The margins of the optic disc and cup are captured by using elliptical fitting around the rough-shaped clusters discovered by FCM, counting on the fact that the disc and cup are of a generally elliptical shape. The authors state that the advantages of their method are a

smaller mean error than k-Mean or standard FCM, and that the method segments both the optic disc and cup "in one stage."

Ganesh Babu's team also used a back propagation neural network for glaucoma detection, but instead of using the neural network to segment the fundus, the network is used as a classifier which is fed the cup-to-disc ratio and two parameters regarding the position of the blood vessels and the width of the optic disc in the four quadrants of the disc, and outputs a prediction regarding the patient's glaucoma status. The neural network classifier was stated to be 90.7% accurate when its source of data was the information from a fundus image, and 89.27% accurate when its source of data was an OCT image (Ganesh Babu 2015). To compare, the mean accuracy for GlauNet, which uses fundus images and bases its diagnosis on a prediction of the cup-to-disc ratio, is 87.0% (see section 5.2.2).

2.4. Inexpensive Medical Computing

A core intent of this project is to create a system which can be installed and operated easily by users in economically depressed areas using inexpensive, commodity hardware. Rather than focusing on lowering the costs to a small-scale end user, much recent research into this field appears to have been focused on the use of cloud computing to lower the costs of large-scale medical research, e.g. the cloud computing system for genome sequencing proposed by Shringarpure et al (Shringarpure 2015). Other research looks to assist patients in remote areas by proposing telemedicine projects, such as the remote electrocardiogram designed by Hsieh et al, which allows the gathering of cardiac data remotely (Hsieh 2012). Still further research focuses on developing ubiquitous medical hardware and software for a first world environment, such as the smart mirror described and partially implemented by Miotto et al (Miotto 2018). Such

systems might be inexpensive in comparison to a full medical suite but are not inexpensive under the definition intended in this document, which is commodity hardware with 4 GB of memory installed. We should, however, not focus on these individual projects, which are used for purposes of illustration, but instead consider the broader issue of affordability in medical computation.

Presumably, many specialized medical software systems will use cloud computing's Platform as a Service and Infrastructure as a Service, rather than Software as a Service, as medical systems for the most part are not standardized commercial software packages that would be preinstalled on a cloud system. However, PaaS and IaaS require in-house specialists who can properly design and implement the cloud system, raising up-front costs (Blanford 2018). And the cloud time itself can be a significant ongoing expense. Take as an example time purchased on AWS, the cloud computing infrastructure owned by Amazon. We will consider the least expensive option, a bare Linux server. The least expensive tier of Linux server which provides 32 GB of memory on AWS costs US$0.301 per hour (Amazon 2020). This is $12.04 each forty-hour workweek the system is in use. It is, however, unrealistic to expect that a cloud system will not require extra time to start and to shut down each day, adding to the hours which must be paid for (Blanford 2018). GlauNet has no continuing costs, as its software is free and open source.

While cloud computing has a relatively small initial cost and a perpetual ongoing cost, telemedicine has both a significant initial setup cost and an ongoing cost. Training to use a telemedicine system is required for computer and medical personnel, and can cost between $200 and $2000. Specialized mobile medical devices cost $5,000 to $10,000. The equipment to support the hardware in the medical office costs $20,000 to $30,000. Telecommunications software costs between $7,000 and $10,000 per patient to be treated in parallel, and the software

costs $1,000 to $1,500 per patient (Escobar 2020). Some telemedicine systems do not feature cost savings to doctors in their sales pitches, but instead promote the systems as "increasing productivity and generating new revenue" - patients who can't get to the doctor's office during normal hours and who would have gone to an alternate medical provider such as an urgent care clinic will instead contact the doctor via the telemedicine system (Medici 2020). Further, telemedicine is not a direct replacement for medical professionals, but is instead a force multiplier. "It is not the intention of telemedicine to reduce the presence of the most valuable medical resources (physicians and specialists)," writes Aurelian Moraru, "but, on contrary, to use these scarce and expensive resources in an intelligent manner and time-saving manner" (Moraru 2017).

Lastly, we will consider ubiquitous medical hardware such as the smart mirror proposed by Miotto. The costs of such systems are difficult or even impossible to discover, as they rely on hardware which does not yet exist outside of computer labs and which are therefore beyond the reach of any doctor or patient. GlauNet, in contrast, is designed to run on 15-year-old hardware using free software.

2.5. Other Research Uses of the Dataset

The Retina Images for Glaucoma Analysis (RIGA) dataset, a collection of fundus images taken from both male and female patients, was made available in 2018. Most medical data corpuses are small, or else are not publicly available. The fundus images in the RIGA dataset were each annotated by six different professional ophthalmologists, marking the locations of the optic disc and cup. The annotations were made with a stylus on a tablet computer, and saved as

images. The RIGA dataset was made available via the University of Michigan's Deep Blue system (Almazroa 2018). The dataset is considered in more detail in Section 3.

Figure 2: Example using RIGA image number 333

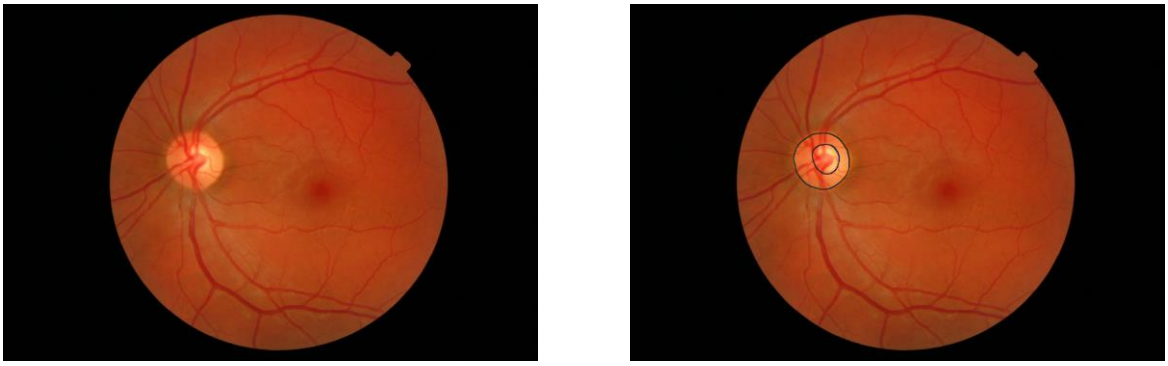

Left: Unannotated image Right: Same image annotated by Annotator 4

Almazroa et al extracted the region of interest around the optic disc from RIGA images and then processed them using a level set function. Almazroa reported that the blood vessels made the level set calculations "inaccurate," so the blood vessels were removed from the image and the image was then "inpaint[ed] using a diffusion process" to infill missing pixels by making them similar to the surrounding, unremoved pixels. After the image was segmented using the level set function, the boundaries of the segmentation were "optimized" to create a smoother contour to the edge. Missing segments of the boundary were then repaired to create a full segmentation. The images were divided into a set used to validate the model, and a set which was not used. If standard deviation for the area of the disc annotation for an image was greater than the mean standard deviation for the areas of all disc annotations, the image was considered an outlier and was not used for training or validation. Segmentations predicted by the model were compared to the disc area and centroid, and those that fell outside a given threshold were marked as incorrect segmentations. The threshold for the MESSIDOR subset of the RIGA

dataset was 1500 incorrect pixels in area or 3 pixels offset for the centroid. The trained model was determined to be 86.6% accurate in calculating the disc area on average across all six annotators (Almazroa 2017). GlauNet is 89.7% accurate on the same measure (see Section 5.2.1).

In 2019 the team of Yu et al used the RIGA dataset as part of the data used to train a U-Net, the same architecture used for this project. As was done in this project and in the network trained by Almazroa, a region of interest was selected surrounding the optic disc and used as the training data. However, Yu's team chose to use a ResNet34 model with pre-trained weights as an encoder instead of starting *de novo* with a fully untrained network as was done in GlauNet. The authors note that their network, using a pre-trained ResNet encoder, trains in two hours versus the ten hours required to train a network from scratch. ResNet is often used to handle the vanishing gradient problem (Dwivedi 2019). The Yu neural network also used 7x7 convolutional layers rather than the smaller 3x3 layers used in GlauNet which capture smaller features.

After being trained, Yu's network outputs "blobs" which were then considered as the segmentation of the image into the cup and disc. This is in contrast to the work I will present in Section 4 showcasing the network design of GlauNet, which generates a complete or nearly-complete segmentation of the fundus image and can capture the C/D ratio without further processing. Further, while GlauNet created six separate models, one for each annotator, Yu's team presumed that a pixel was labeled as "disc" or "cup" only if three of the six annotators labeled it so, and then created a combined network using this majority-rule technique. Yu considered the segmentation task "as a pixel-level classification problem" and therefore "use[d] binary cross entropy logistic loss as the loss function." My network, in contrast, considers the

segmentation task as a problem of classifying two disjoint sets, and therefore uses the Jaccard Distance as its loss function.

Yu's model was trained for 30 epochs, while the six models that make up the trained networks in GlauNet were trained for between 847 and 1444 epochs. Yu's team reported an average Jaccard Index[2] of 94.80% for segmentation of the disc and 79.40% for segmentation of the cup (Yu 2019). The Jaccard indices for the segmentations by GlauNet's models were calculated, as well as the index for the networks as an aggregate (see Section 5.2.3).

The best GlauNet model overall, Model A, has a mean Jaccard Index of 91.20% for the area of the optic disc and 81.26% for the area of the cup. This is roughly equivalent to Yu's method, which is slightly better at this metric for the area of the disc and slightly worse of the area of the cup. The overall GlauNet model has a mean Jaccard Index of 90.59% for the area of the disc and 75.85% for the cup. This is noticeably worse than Yu's method. However, as noted, Yu's team created aggregate segmentations and trained against them, which artificially changes the problem.

The next section discusses the RIGA dataset and the work done to prepare it to use in training a neural network.

[2] The Jaccard Index measures how closely two sets intersect, and is detailed further in section 4.7.1.

3. Data

3.1. Cup-to-Disc Ratio

The normal optic disc is approximately 1.5 mm in diameter (Fanelli 2013) and the disc can vary in area from 1.25 to 4.0 square millimeters in area, with the mode being between 2.0 and 2.25 square millimeters (Hayamizu 2013). The ratio of the diameters of the cup and the disc is a valuable parameter for diagnosis of glaucoma in both the early and the late stage of the disease, because the cup-to-disc ratio in glaucomatous eyes is significantly larger than is found in non-glaucomatous eyes. Furthermore, the cup-to-disc ratio is larger in eyes that present with late stage glaucoma than in eyes with early stage glaucoma, which allows for tracking the process of the disease over time (Okimoto 2015).

As previously stated, the cup-to-disc ratio is among several morphometric variables of the eye which can be used to diagnose glaucoma, and these morphometric variables are difficult for even trained specialists to determine with precision. Almazroa at al considered six trained ophthalmologists who annotated the optic cup and disc on identical sets of fundus images, with agreement of the area of the optic disc, the centroid of the optic disc, and the C/D ratio considered "by comparing the analysis of each observer with the median result of the other five," and with annotations which were beyond the mean standard deviation discarded as outliers. Almazroa found agreement among the six annotators' measurements, which had already been chosen for similarity by removing outliers, was at best 63.4% (Almazroa 2017). An untrained annotator would be expected to perform even worse than this, which leads to an obvious issue in areas of the world which are underserved by medical professionals.

To measure the cup-to-disc ratio, one must first detect the cup and the disc, which entails segmenting the retina in the back of the eye into three classes: the cup, the disc, and what we will

call the background - all other features in the retina. The cup-to-disc ratio can then be calculated using these features.

Automating this process requires a corpus of images which have been manually annotated by specialists. Such a manual annotation is possible using fundus images, which are images of the retina in the back of the eye, captured with the eye either dilated or undilated. Figure 3 shows an example of such a fundus image. The optic disc is within the pale region, center-right, and the optic cup is inside the optic disc but is not easily separated by an untrained person; Figure 3 shows the separation by a trained ophthalmologist.

Figure 3: RIGA fundus image of retina

Fortunately, such a corpus of annotated fundus images exists, the Retinal fundus Images for Glaucoma Analysis (RIGA) dataset (Almazroa 2018). The dataset consists of 750 images of varying dimensions ranging from 1440x960 to 2743x1936 pixels. The images are in three sets, based on which medical center the images were sourced from. The smallest set, from the Magrabia medical center, was not used as its images are cropped from the full fundus image. The second-smallest set, from the Bin Rushed medical center, were in lossy jpeg format and were unsuited to the method used to capture the annotations. The largest set, consisting of lossless tiff images sourced from the Messidor center, was used. The Messidor images which

were 1440x960 were chosen, giving 163 fundus images and 978 annotated images, each 9.8 MB in size.

The RIGA dataset consists of sets of seven images: one "base" fundus image which captures the unannotated retina, and six annotated images, one for each ophthalmologist. The annotations take the form of thin lines which outline the edge of the cup and the disc as determined by the annotator. The cup and the disc are both marked on the same image, making it necessary to differentiate them before segmentation could proceed.

Each image in the RIGA dataset has been manually annotated by "six experienced ophthalmologists individually using a tablet [computer] and a precise pen." An example of an annotated image is shown in Figure 4. The six annotators were not in agreement with one another as to the extent or location of the cup or the disc. This interannotator disagreement is, however, not at all unusual; two ophthalmologists can disagree regarding these parameters since the positions of the edges of the cup and the disc are subjective measures which can be interpreted differently between annotators (Fanelli 2013). Figure 5 presents the region of interest around the optic cup and disc

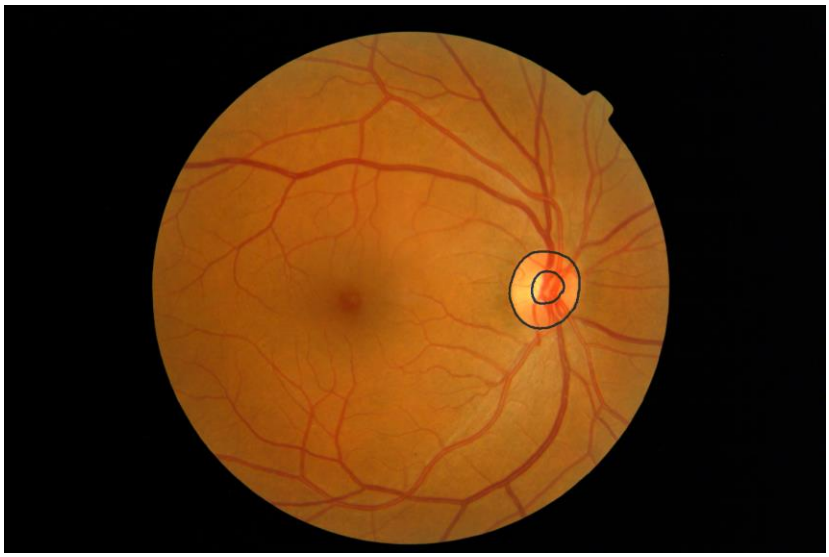

Figure 4: RIGA annotated image

in RIGA MESSIDOR image 200, and the annotations by three of the ophthalmologists, to illustrate the disagreement among them.

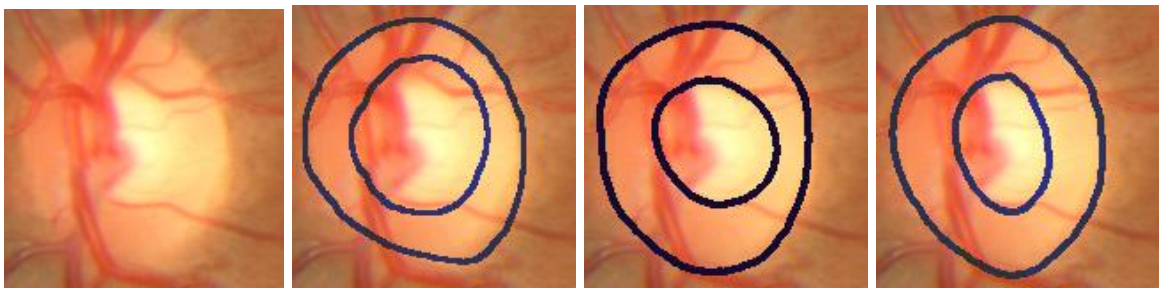

Figure 5: RIGA fundus image and annotations of the same image by three annotators

Almazroa, et al, considered the accuracy of the six annotators in the RIGA dataset. They defined accuracy to be an annotation whose standard deviation falls within the mean standard deviation among the all annotated images the authors surveyed. They found that, in the RIGA dataset, the best accuracy by any of the six annotators was 88.7%, and the lowest accuracy was 75.7%. Annotation of the optic disc by the six annotators was notably better than their annotation of the cup, "due to the clarity of the disc boundaries" (Almazroa, 2016).

3.2. Extracting Annotations

RIGA is encoded as TIFF images. A TIFF image consists of a three-dimensional array in which two dimensions of the array are the X and Y coordinate plane of pixels in the image itself and the third dimension is a set of three integers which represent the coordinate of a pixel's color in RGB space, with zero being the absence of a given color and with [0,0,0] therefore being black.

The virtual pens used by the annotators were not all the same color, so it was not possible to simply search for pixels containing the vector for the annotation color and separate them out to

discover the annotations. Instead, to separate the annotations for the cup and the disc, a program was written in Python which opens an annotated image and an unannotated base image, converts them to NumPy arrays using the Pillow image-processing library, and then subtracts the unannotated base image from the annotated image element-wise. This leaves the annotations as the difference, and all other pixels as black. Because both the base and annotated images are lossless TIFFs, there is no artifacting left behind to confuse the process. The algorithm is presented in Algorithm 1:

```
for each fundus image:
   for each annotator:
      img_fundus ← open fundus image
      img_annotation ← open related annotated image
      fundus ← convert img_fundus into NumPy array
      annotation ← convert img_annotation into NumPy array
      diff_tmp ← pixelwise subtract annotation from fundus
      diff ← sum color space in each pixel of diff_temp
      outer_top ← index of first row with non-zero data
      outer_bottom ← index of last row with non-zero data
      outer_left ← index of first column with non-zero data
      outer_right ← index of last column with non-zero data
      center_pt ← ([outer_left+outer_right]/2 ,
           [outer_top+outer_bottom]/2)
      append these outer points to outer_list
      rotate image around center_pt
      discover new outer points, append to outer_list
      set elements within n of each point in outer_list to 0
      inner_top ← index of first row with non-zero data
      inner_bottom ← index of last row with non-zero data
      inner_left ← index of first column with non-zero data
      inner_right ← index of last column with non-zero data
      append these inner points to inner_list
```

```
center_pt ← ([inner_left+inner_right]/2 ,
     [inner_top+inner_bottom]/2)
rotate image around center_pt
discover new inner points, append to inner_list
export inner_list and outer_list to R to create bitmap
     encoding the captured annotations
```

Algorithm 1: Capturing annotations from human-annotated images

Due to TIFF using a vector of three integers to define a location in its color space, and black being [0,0,0], it is possible to add together the three integers of the RGB vector into a single integer, after which we will find that a black pixel will be represented by zero and all non-black colors will be represented by positive integers. This allows simple logical processing to find the edges of the annotations - we find columns and rows which contain non-zero integers, then find the minima and maxima for the row and column coordinates. A row minimum is the top of a given annotation's bounding box, while a row maximum is the bottom of the bounding box. Similarly, column minima and maxima locate the left and right edges of the bounding box, respectively.

The center of the annotation is located using the averages of the row and column minima and maxima, then the entire image is iteratively rotated around this center. The row and column maxima and minima are found

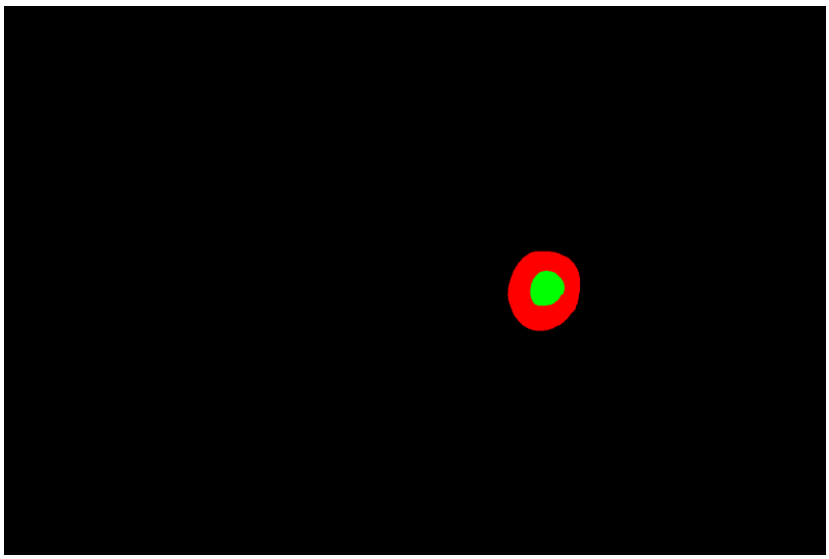

Figure 6: Captured annotation mask

Black: background; Red: optic disc; Green: optic cup

along the row and column of the center point at each rotation, which allows us to find points along the annotation that define it as a polygon of similar shape to the original manual annotation. After the program captured the annotation marking the greatest extent of the optic disc, the annotation for the optic disc was removed from the in-memory copy of the annotation image and the process was repeated to locate a polygon contiguous with the annotation of the extent of the optic cup.

The process above failed to capture the perimeter points of the segmentations in some cases. These annotated images were removed from the dataset. Some captures included annotations which extended beyond the 160x160 captured area, and were also removed. The number of removals is detailed in Table 2.

Annotator	Failed Captures	Oversize Captures	Total Removed
1	5	2	7
2	28	7	35
3	1	0	1
4	29	4	33
5	8	11	19
6	15	8	23

Table 2: Failed and removed annotation captures by annotator out of 163 images

The points on the polygon were exported to a program in the R language, which has fast vector-based processing at its core (Jones 2014). This allows for quickly generating a set of data points representing the class of each pixel and saving it to a file.

After the annotations were captured by the Python and R programs, the classes were programmatically processed and counted. The "background" class makes up, on average, 98.9% of the pixels in a fundus image, while on average the optical disc makes up 0.9% of the image and the optical cup makes up just 0.3% of the image.

The next section introduces neural networks, and presents a system that automatically learns how to identify a cup and disc, when given data from this section as input. Overall, 860 images will be passed to this next module.

4. Neural Network Architecture

In this section, I present an introduction to image segmentation, conventional neural networks, convolutional neural networks, and U-Net. I describe an issue with class imbalance in the dataset and how it was corrected by capturing a region of interest in the images around the optic cup and disc.

4.1. Image Segmentation

To make decisions or judgements regarding medical images, one often must first separate the areas of interest from the background and from each other, a process called image segmentation (Bankman 2009). In image segmentation, a process - carried out either by humans or machines - splits an image up into "meaningful but non-overlapping regions" (He 2018).

Image segmentation can be manual, semiautomatic, or automatic, in a spectrum from a workflow which requires human work at every step to a workflow in which a computer system takes in unsegmented data and outputs segmented data. Segmentation can also be divided into region segmentation and edge-based segmentation; in region segmentation, the system searches for regions which match "a given homogeneity criterion," whereas edge-based segmentation discovers edges between regions where the regions have sufficiently different attributes (Bankman 2009). The method discussed in this work is semiautomatic and regional.

4.2. A Brief Primer on Neural Networks

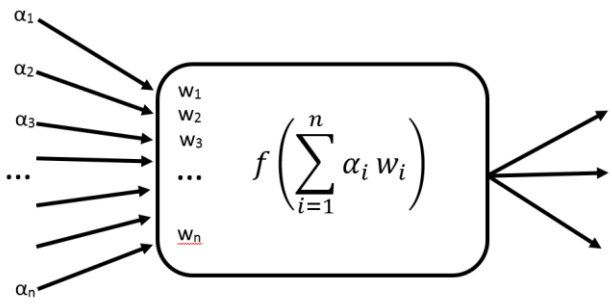

Figure 7: Conceptual design of a neural network neuron

α: incoming value,
w: weight applied to incoming value,
f: activation function

Neural networks are learning systems inspired by the form of the brain, with neurons connected to one another and influencing each other (Yamamoto 2011). Each artificial neuron, sometimes called a perceptron, in a neural network receives one or more inputs, applies a weight to each input, sums the weighted inputs, and then applies an activation function to the sum; this is illustrated in Figure 7. The result of the activation function is sent out via outgoing links to either one or more neurons, or as a part of the final output from the network.

Neurons are arranged into layers - an input layer, one or more hidden layers, and an output layer - which feed into one another; see Figure 8, which illustrates a fully connected neural network in which each neuron in a layer is connected to every neuron in the next layer. The example network in Figure 8 takes in four numbers and emits two numbers. Numeric data - such as the numbers representing the colors of individual pixels, as in Figure 9 - is fed into the input layer, which processes it by having each neuron in the input layer apply its

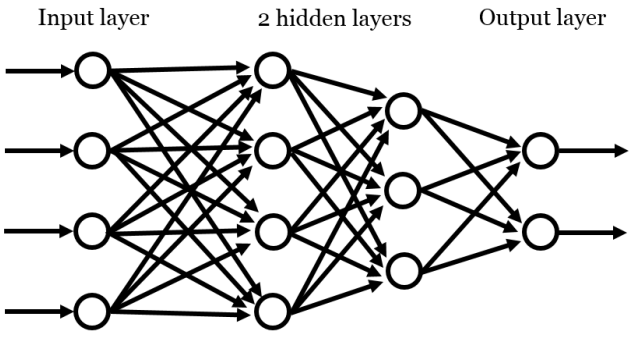

Figure 8: Fully connected neural network design
Each circle is a neuron.

weights and activation function. The output of each neuron in the input layer is fed to one or more neurons in the first hidden layer. The neurons in the first hidden layer apply their weights and activation functions to the inputs from the input layer, and feed their outputs to the second hidden layer. The second hidden layer processes the inputs from the first hidden layer in the same way, then passes it to the output layer, which processes it. The neurons in the output layer deliver their outputs out to the outside world as the prediction from the neural network.

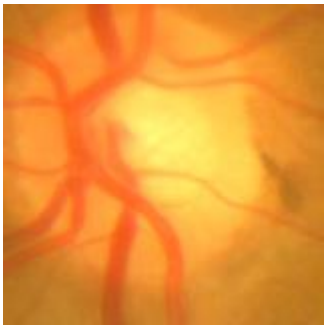

Figure 9: Sample input data: region of interest captured from RIGA MESSIDOR image 193

A neural network of more than one layer can represent "any continuous function, and even discontinuous functions" (Russel 2010). Such networks can discover useful features in an image by creating feature maps within each hidden layer (Cernazanu-Glavan 2013).

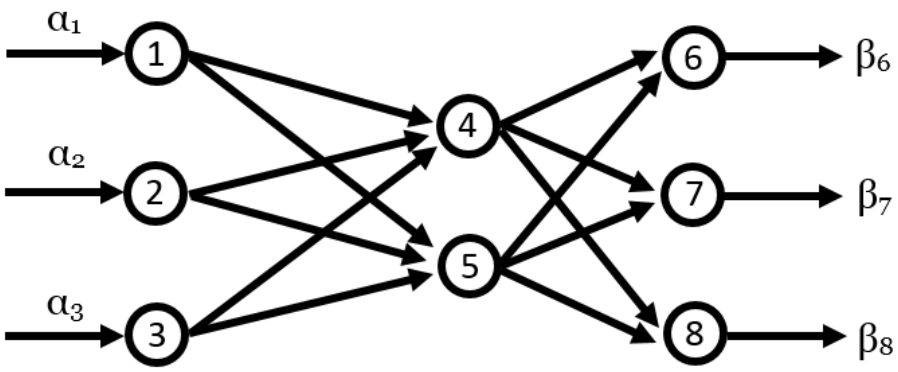

Figure 10: Example neural network

Putting data into the network's input layer and then running the data through the layers of artificial neurons, leading to an output at the output layer, perhaps a binary classification or a matrix representing an image segmentation, is called the feed-forward process. For the simple network illustrated in Figure 10, the inputs are denoted as α_n and the outputs are denoted as β_n,

where n is the number of the neuron taking the input or delivering the output. If the activation function of neuron n is $f_n()$, and $w_{x,y}$ is the weight given by node x to the input from node y, the output of each neuron at the output layer can be derived:

$$\beta_1 = f_1(w_{1,0}\alpha_1)$$

$$\beta_2 = f_2(w_{2,0}\alpha_2)$$

$$\beta_3 = f_3(w_{3,0}\alpha_3)$$

The outputs of the input layer are then clearly:

$$\beta_n = f_n(w_{n,0}\alpha_n)$$

These three outputs act as inputs to the hidden layer. The outputs of neurons 4 and 5 are:

$$\beta_4 = f_4(w_{4,1}\beta_1 + w_{4,2}\beta_2 + w_{4,3}\beta_3)$$

$$= f_4\left(\sum_{n=1}^{3} w_{4,n}\beta_n\right)$$

$$= f_4\left(\sum_{n=1}^{3}[w_{4,n}f_n(w_{4,n}\alpha_n)]\right)$$

Similarly,

$$\beta_5 = f_5\left(\sum_{n=1}^{3}[w_{5,n}f_n(w_{5,n}\alpha_n)]\right)$$

The output from neuron 6 is then:

$$\beta_6 = f_6(w_{6,4}\beta_4 + w_{6,5}\beta_5)$$

$$= f_6\left(\sum_{m=4}^{5} w_{6,m}\beta_m\right)$$

$$= f_6\left(\sum_{m=4}^{5} w_{6,m} f_m\left(\sum_{n=1}^{3}\left[w_{m,n} f_n\left(w_{m,n}\alpha_n\right)\right]\right)\right)$$

The general formula for the three output neurons in the output layer is:

$$\beta_r = f_r\left(\sum_{m=4}^{5} w_{r,m} f_m\left(\sum_{n=1}^{3}\left[w_{m,n} f_n\left(w_{m,n}\alpha_n\right)\right]\right)\right)$$

The output of the neural network is a vector of all three outputs from the neurons in the output layer.

Training a neural network is the process of discovering the weights which best approximate a solution to the problem at hand. After feed-forward, the network can read its output layer, calculate a loss, and perform back-propagation to correct its weights. In back-propagation, the network will update the weights on its neurons in an attempt to decrease its loss and come closer to a correct, generalizable network. To back propagate, the network will run the feed-forward process; determine the error of its output by comparing the calculated and expected outputs using a loss function; and perform the feed forward operations backward, during which it will slightly correct each of the weights. Each update via back-propagation is intended to make the network's model more correct with respect to the measured loss, although this can fail in the event of overfitting. When the loss falls below some defined point, or when a given amount of work has been put into the process of training, the network finishes training and saves off its last (or, in the case of certain sufficiently advanced training methods, its most correct) network weights.

The method of backpropagation used today was proposed by Rumelhart, Hinton, and Williams (Rumelhart 1986). It begins by noting that for a "fixed, finite set of input-output cases," which exists for any reasonable machine learning training, the error can be calculated by comparing the model's prediction and the ground truth as vectors. For the index of input-output

pairs, or cases, c; the index of output units j; the predicted state of output y; and the ground truth or "desired state" d; they give the error, E, as:

$$E = \frac{1}{2}\sum_{c}\sum_{j}\left(y_{j,c} - d_{j,c}\right)^2$$

In backpropagation we calculate the partial derivative $\partial E/\partial y$ for each output unit, giving:

$$\frac{\partial \mathrm{E}}{\partial y_j} = y_j - d_j$$

Modern systems supporting neural networks, such as TensorFlow, automate the process of backpropagation and the correction of weights.

When one attempts to use a neural network to work with image data, the number of weights rapidly increases; for a 200x200 image with color information stored as red, green, and blue intensities, a single fully-connected neuron will have 120,000 weights (Li 2020). To solve this issue, Convolutional Neural Networks were proposed.

4.3. Convolutional Neural Networks

The project at hand involves discovering features in images, which is not a strength of traditional neural networks. Convolutional neural networks (CNNs), which were developed from traditional neural networks by LeCun and Simnard and were inspired by the configuration of an animal's visual cortex, retain the relationships among pixels in 2D or 3D space. This allows a CNN to discover features within an image (Cernazanu-Glavan 2013, Rezaul 2018) while decreasing the memory footprint of the network by reducing the number of weights in the network using weight sharing among kernel filters (Hao 2020).

The heart of a CNN is the convolutional layer. A convolutional layer uses the outputs from neurons that are connected to a receptive field – a small, (usually) square region of the input from the previous layer. The convolutional layer calculates a dot product between the weights of these neurons and the receptive field. A convolutional layer has three-dimensional volume; if 64 filters are chosen for a layer with an n x m spatial size, the layer will be n x m x 64 (Li 2020).

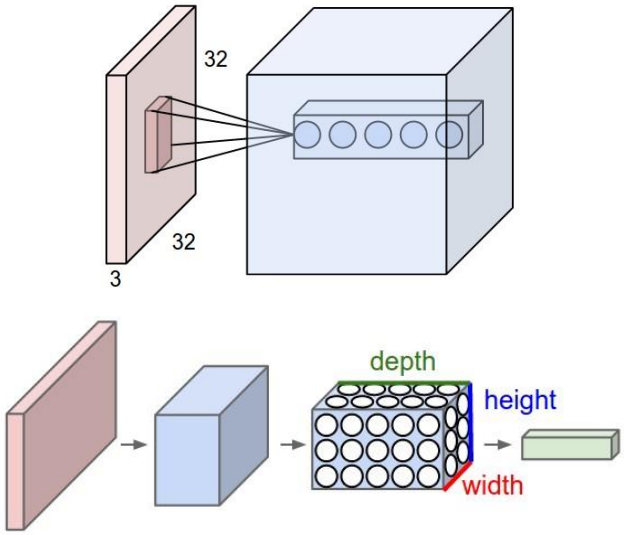

Figure 11: CNN convolutional layer

Images from Github repository of Stanford CS class CS231n, made available under the free MIT License.

The convolutional layer consists conceptually of a set of feature maps, each of which is generated by a kernel filter. The kernel filter is moved across the image stepwise, in effect "looking" at each segment of the image within its receptive field in turn to search for its given feature. Each feature map learns to capture an element of an image, such as an edge or a gradient of color. These feature maps will feed into later layers in the network, allowing the network to aggregate and capture more and more complex features deeper into itself; the model thereby discovers low-level features in earlier layers and builds them into high-level features in later layers. Because feature maps are not fixed to a given point in the input data, they can be used to recognize a pattern anywhere within an image; in contrast, a traditional neural network which learns a feature will only detect it in a static position within an image. This allows CNNs to generalize more correctly than traditional neural networks do (Rezaul 2018)

Working between the convolutional layers are pooling layers. These layers decrease the size of their inputs in the height and width dimensions. A pooling layer does not decrease the size of its input in the depth dimension. Because the pooling layer outputs less data than it receives, it lowers the amount of calculation required for the network, and also decreases overfitting. A pooling layer typically will view a set of pixels and take the maximum value from among them (Li 2020), as Figure 12 demonstrates.

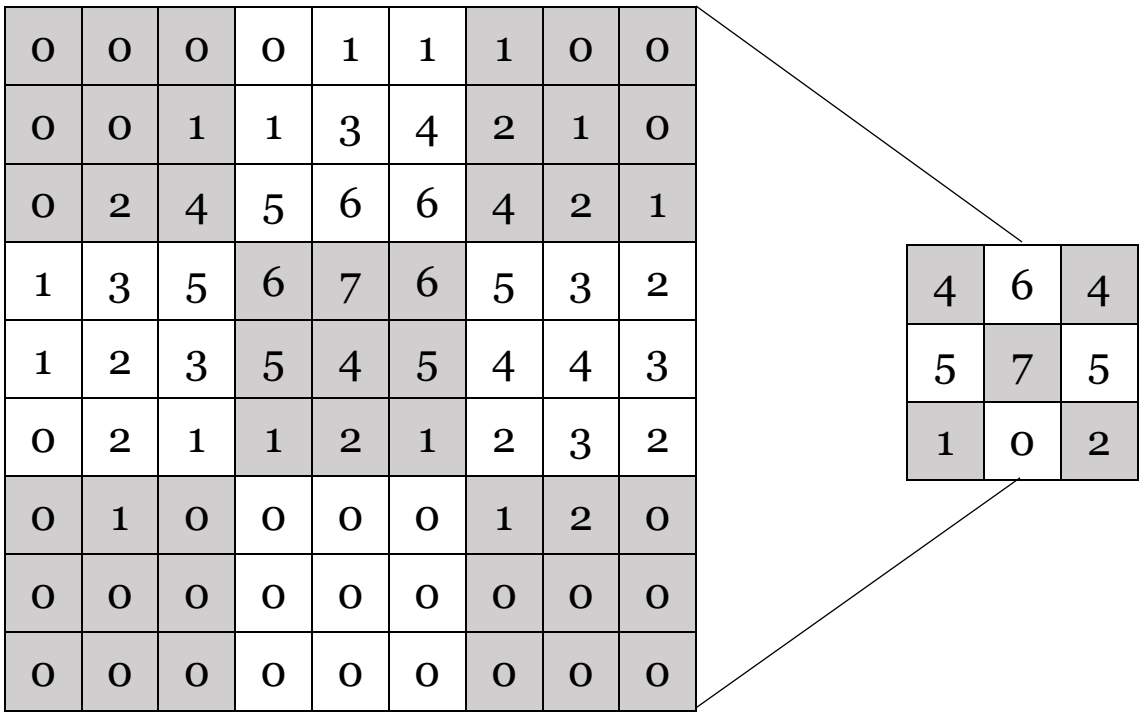

Figure 12: A 3 x 3 pooling operation with a stride of 3

A version of CNN called U-Net was proposed in 2015 by Ronneberger, Fischer, and Brox, with the intention that the network would work well for image segmentation tasks (Ronneberger 2015). A U-Net architecture was used in GlauNet. We will discuss its specific architecture in the next subsection.

4.4. U-Net

The task of segmenting fundus images to capture the locations of the cup and disc requires precision and speed, and also requires the ability to capture a generalizable model without the use of immense data corpuses which are not available for this project. Fortunately, a machine learning architecture which matches these requirements exists: U-Net. The U-Net design is known to have "high capability for high spatial resolution prediction task[s]" (Chen 2018). The U-Net architecture also allows for training with fewer image samples, as the network transfers features from the lower levels of the network to higher levels, allowing the use of both fine detail at the lower levels and semantic features at the higher levels; this helps to overcome a paucity of training data (Zhang 2017).

At its simplest, a U-Net can be thought of as shrinking the image while capturing fine shape, color, or position detail, then growing or upsampling the image while capturing semantic information using the fine detail. A U-Net is formed of successive sets of convolutional layers and pooling layers which shrink the width and height of the data but increase its depth as we move deeper into the network. Once the full depth of the network is reached, the network switches to upsampling and grows the width and height of the network while shrinking its depth, until the output is the same shape as the original input had been. Data from earlier in the network are copied forward into later layers, so that features discovered earlier in the process, when fine details are still available, are not lost to the model (Ronneberger 2015). Thus, location within the image and semantic context are both captured, which is advantageous for image segmentation (Alom 2019).

We will illustrate a U-Net while describing its implementation in GlauNet. The network is conceptually made of blocks of convolutional, pooling, upsampling, and dropout layers.[3] A dropout layer randomly sets inputs to zero during training. Inputs which are not changed are "scaled up…so that the sum over inputs is not changed" (TensorFlow 2020). Dropout was added to the network to prevent overfitting.

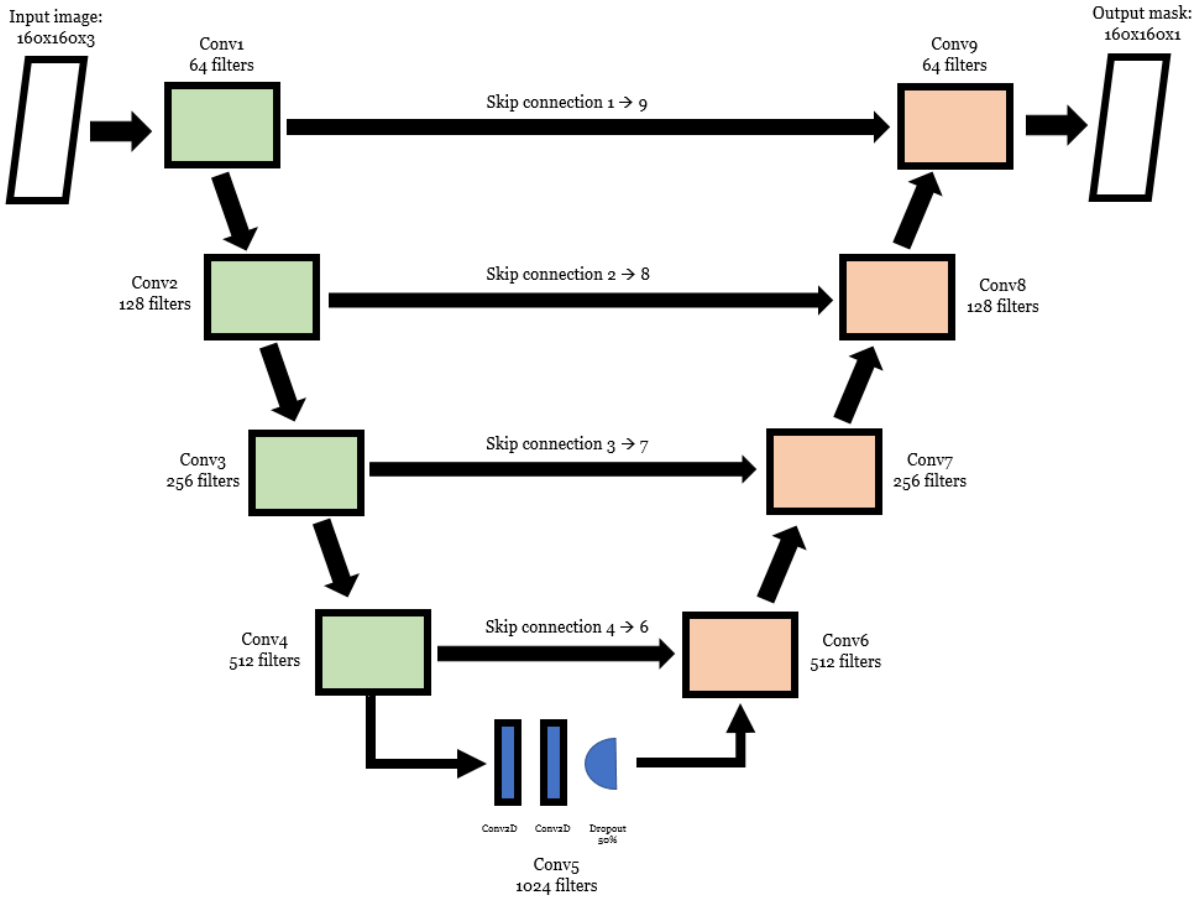

Figure 13: GlauNet's U-Net architecture implementation

The architecture of GlauNet is pictured in Figure 13. As connections in the network go "down," the downsampling makes the data being processed smaller in the x and y directions, and more filters are added to look for more features. A "skip" connection takes the output from a

[3] This base U-Net architecture is by Zhixu Hao (Hao 2018).

convolutional layer in each down block is sent over to an up block at the same "level," where the down block's output is concatenated with the up blocks input after upsampling, and the concatenated data is fed into the up block for processing. This skip connection makes certain that some fine details are not lost by the downsampling process, as the detail is replicated over to the up blocks. The "bottom" of the network is two convolutional layers and a 50% dropout layer. The heaviest dropout is at the bottom, as fine detail has been entirely lost at this level.

The abstracted details from Figure 13 are shown in Figures 14 and 15, below. Figure 14 displays a downward block within GlauNet's architecture, and Figure 15 shows an upward block.

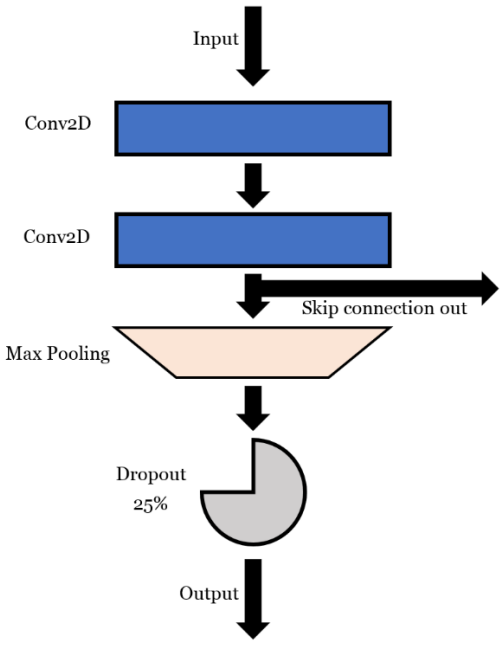

Figure 14: Architecture of GlauNet's downward blocks

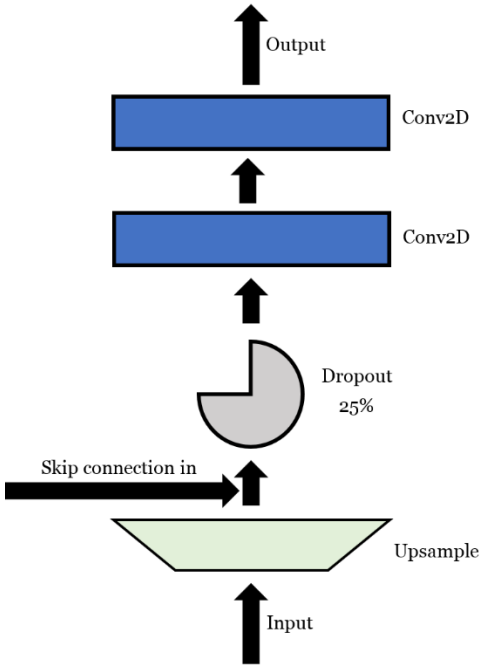

Figure 15: Architecture of GlauNet's upward blocks

The downward block takes in an input from a previous block, runs it through a convolutional layer, then through another convolutional layer. The output of the second layer is sent both to a "skip" connection to one of the up blocks, and down to a pooling layer. The

pooling layer contracts the spatial dimensions (x and y) of its inputs by half. This is fed into a dropout layer which inactivates 25% of the inputs, and feeds to an output to the next block.

The upward block, shown in Figure 15, takes input and upsamples it. It is possible to use a simple upsample, such as expanding a single pixel into an identical set of four pixels to double the size of an image. However, GlauNet uses Keras's convolutional upsampling layer, which both upsizes the incoming data and has weights which can be corrected (unlike simple upsampling, which is non-correctable).

The upsampled data then are concatenated with data from the skip connection to the down block on the same layer as this up block. This concatenated data is fed through a dropout layer which inactivates 25% of inputs to the first convolutional layer. The two convolutional layers process the data, and feed it out to the next block.

The last "block" is the output layer, which presents a 160x160 bitmap predicting where the optic disc is to be found in the input.

4.4.1. U-Net Comparison

U-Net has disadvantages when compared with other neural networks. It is a quite large and deep network, leading to an extremely large memory footprint. The saved weights file for one GlauNet model is 355 MB, and GlauNet uses six such models. Making a prediction with a U-Net is relatively fast; I demonstrate in Section 6.2 that making predicted segmentations for each of the six models with the U-Net within GlauNet takes a mean of seven seconds. However, loading the models into memory so that these predictions can be made takes nearly a minute.

Further, U-Nets can have problems when the segmentable area of a class is small in comparison to the full size of the image, and for medical image segmentation, tissues which are

similar to their surroundings can cause issues for U-Nets (Song 2019).[4] The segmentable area being small in comparison to the full size of the input is a problem of class imbalance, and the next subsection discusses the actions undertaken to handle this issue.

4.5. Class Imbalance

There is, one must note, a significant imbalance in the number of instances of each class within a fundus image. The full retina of the adult human eye is 1094 square millimeters in area, although a fundus camera does not capture an image of the entire retina (Kolb 2017), and as stated earlier in this section, the optic disc – which is larger than the cup – averages between 2.0 and 2.25 square millimeters in area. This difference in sizes between the physiological regions leads to a class imbalance in the annotated image.

In a full-sized image, the "background" class makes up, on average, 98.9% of the pixels in a fundus image, while on average the optical disc makes up 0.9% of the image and the optical cup makes up just 0.3% of the image. We can see that the number of pixels in the cup class and the number of pixels in the disc class are very roughly equivalent - within a factor of three - but the number of pixels in the background class is larger than the number in the cup or disc by several orders of magnitude. An imbalance between classes negatively impacts the training and generalization of convolutional neural networks. One method for correcting this imbalance is to preprocess the data to remove the imbalance by removing instances of the majority class, a process called undersampling (Buda 2018).

To achieve undersampling and thereby roughly balance the number of pixel instances belonging to each of the three classes, a localized section of the image was captured, as described

[4] In the initial design phase of this project, artificially created random "tricolor flags" were made as an input to a U-Net, to see how rapidly a U-Net would train and to give a first impression of what learning rate would be required.

in Section 4.6. Using the known locations of the annotations, a 160 by 160 pixel section of each base image and each captured annotation, containing the annotated area, was clipped from the full TIFF images and annotation files.

This left the number of pixels in each image of each class roughly in balance. The localized sections of the captured annotations were processed and counted, and the background accounted for on average 38.7% of the pixels (minimum 16.1%, maximum 57.4%), the optic disc accounted on average for 46.0% of the pixels (minimum 31.9%, maximum 65.1%), and the optic cup accounted for 15.3% of the pixels (minimum 4.2%, maximum 28.4%).

The localized images and annotation masks were used to train and validate the network.

4.6. Image Preprocessing

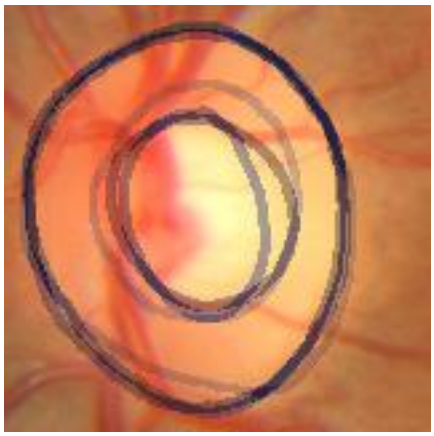

Figure 16: Three annotations of RIGA MESSDOR image 200 overlaid to demonstrate interannotator disagreement

As noted in section III.1, two ophthalmologists can disagree regarding the extent, location, or shape of the cup or the disc. This is, however, not at all unusual; two ophthalmologists can disagree regarding these parameters since the positions of the edges of the cup and the disc are subjective measures which can be interpreted differently between annotators (Fanelli, 2013). A sample of such annotation differences is shown in Figure 16, which depicts annotations of the same fundus image by three different annotators overlaid atop one another to make the disagreement among their annotations more apparent. Recall that the agreement among annotators, even with the outliers among their annotations removed, is at best 63.4% (see Section 3.1).

To handle these inter-annotator discrepancies, it was decided to consider the six RIGA annotators separately, rather than to attempt to build a network which would segment an image using all the annotators' segmentations as a group corpus, as the use of a group corpus would lead to a trained network which would not align with any of the annotators.

After the annotations were captured by the Python and R programs, the classes were programmatically processed and the pixels belonging to each class were counted. Table 3 details the average number of pixels in each class per image in fundus images annotated by Annotator 3, and the percentage of the total in each class.

	Avg. Pixels per Image	Minimum Class Frequency (%)	Avg. Class Frequency (%)	Maximum Class Frequency (%)
Background	1,366,539.3	98.3	98.8	99.2
Optical Disc	11,948.3	0.5	0.9	1.3
Optical Cup	3,912.4	0.1	0.3	0.5

Table 3: Number of pixels across Annotator 3's images, for full-sized images

The "background" class makes up, on average, 98.8% of the pixels in a fundus image, while on average the optical disc makes up 0.9% of the image and the optical cup makes up just 0.3% of the image. We can see that the number of pixels in the cup class and the number of pixels in the disc class are very roughly equivalent - within a factor of three - but the number of pixels in the background class is larger than the number in the cup or disc by several orders of magnitude. An imbalance between classes negatively impacts the training and generalization of convolutional neural networks. One method for correcting this imbalance is to preprocess the data to remove the imbalance by removing instances of the majority class, a process called undersampling (Buda, 2018).

To achieve undersampling and thereby roughly balance the number of pixel instances belonging to each of the three classes, a section of the image localized to the region of interest was automatically captured. Using the locations of the annotations, a 160 by 160 pixel section of each fundus image and each captured annotation, containing the region of the optic disc and optic cup, was clipped from the full TIFF images and annotation NumPy arrays. The 160x160 pixel size for the region if interest was chosen by measuring the optic disc size in a randomly chosen subset of the Annotator 3 annotations. The region of interest was captured using Algorithm 2:

```
for each fundus image:
   for each annotator:
      open fundus image
      open related annotated image
      top ← index of first row containing annotation data
      left ← index of first column containing annotation
      subimage ← columns left...(left+160) and rows
                 top...(top+160) from fundus image
      save subimage as a TIFF
      submatrix ← columns left...(left+160) and rows
                  top...(top+160) from NumPy array
      save submatrix as a NumPy array
```

Algorithm 2: Capturing the region of interest in images

Some regions of interest were more than 160x160 pixels in size, and were removed during visual checking of the output. Capturing the region of interest around the optic disc left the number of pixels in each region roughly in balance in each region of interest image. The number of pixels was counted in those localized images which had been annotated by Annotator 3, and the number of pixels in each class was calculated. The background accounted for on average 38.3% of the pixels (minimum 12.9%, maximum 57.4%), the optic disc accounted on average for 46.4% of the pixels (minimum 31.9%, maximum 65.1%), and the optic cup accounted for 15.3% of the pixels (minimum 4.2%, maximum 23.4%). This is summarized in Table 4.

	Avg. Pixels per Image	Minimum Class Frequency (%)	Avg. Class Frequency (%)	Maximum Class Frequency (%)
Background	9,796.9	12.9	38.3	57.4
Optical Disc	11,886.8	31.9	46.4	65.1
Optical Cup	3,916.2	4.2	15.3	28.4

Table 4: Number of pixels across Annotator 3's images, for localized images

The localized images and annotation masks were used to train and validate the network.

4.7. Hyperparameters

4.7.1. Network-Scale Hyperparameters

An untrained neural network is characterized by its parameters and its hyperparameters, which work together to define how the network will learn, and whether it will learn at all. The parameters are the settings which are calculated during the learning process, such as weights within the neuron, while the hyperparameters are those settings chosen by the network's creator

(Alto 2019). A network's hyperparameters of importance are its activation function, its initializer, its loss function, its optimizer, and its batch size.

A neuron's activation function converts the summed weighted inputs of the node into its output. GlauNet uses the rectified linear unit (ReLU) activation function:

$$\text{ReLU}(x) = \begin{cases} x & if\ x > 0 \\ 0 & if\ x \leq 0 \end{cases}$$

GlauNet uses the ReLU activation function both because it has been found empirically to function well as the activation function for neural networks, and because it is simple and therefore fast to calculate, which facilitates faster learning (Lu 2019, Arnekvist 2020).

A neural network must be initialized with weights before it begins training. An incorrectly chosen initializer can cause a network to train more slowly, or entirely fail to train. It is possible – and was in the past popular – to initialize a neural network with data drawn from Gaussian distributions with a fixed standard deviation, but this method cannot be used when one is training a deep network (He 2015). An improperly initialized layer will either diminish or overamplify the signal fed into it, leading to an incorrectly identified gradient and an incorrect output (Mishkin 2016). In 2015 He, et al, recommended initializing the weights in a deep neural network's neuron by drawing from Gaussian distributions using a standard deviation which relates to the number of inputs rather than being fixed (He 2005). To make it more likely that the network will train properly, GlauNet uses this He normal initializer, which is built into TensorFlow. Note that in TensorFlow it is possible to define an initializer for each layer rather than for the entire network, but He normalization was used for the entire network for this project as it is the correct initializer in this application.

Perhaps the most important choice in a neural network is which loss function to use. A loss function describes how closely a model's output relates to ground truth, and training a neural

network is in its most basic definition the process of finding a set of weights for the network which create the smallest loss. After each training batch is completed, the correct and calculated output from the network are compared and a loss is calculated. A loss function will delineate how closely a given output of the network matches to the ground truth. As an example, pixel-wise cross entropy is a popular loss function for image segmentation. More than half of the machine learning image segmentation papers in the proceedings of the medical imaging machine learning conference, MICCAI 2018, used pixel-wise cross entropy loss. Bertels, et al, consider cross entropy loss, as well as Jaccard and Dice loss, which can also be used as loss functions for training a neural network for image segmentation. The authors test cross entropy, Jaccard, and Dice as the loss functions for a U-Net architecture for segmentation of several image corpuses and found that cross entropy is inferior to both Dice and Jaccard, as well as finding that cross entropy is worse at segmenting classes with small relative size. They also demonstrate mathematically that Dice and Jaccard losses can approximate one another, while cross entropy can approximate neither, and that there is no statistical difference in efficacy between the Dice and Jaccard loss functions so either one may be chosen (Bertels 2019).

This project uses the Jaccard Distance, the involution of Intersection over Union (IOU), which measures the similarity between sets. Segmentations of the fundus images can be considered as sets (Iglovikov 2018; Bertels 2019). Per Iglovikov et al, the Jaccard index for sets S and T, *L(S,T)*, is calculated as:

$$\mathrm{L(S,\ T)} = \frac{Area\ of\ Intersection}{Area\ of\ Union} = \frac{|S \cap T|}{|S \cup T|} = \frac{|S \cap T|}{|S| + |T| - |S \cap T|}$$

The Jaccard Distance is then *1 – L(S,T)*. Per Kayalibay, the Jaccard Distance is also equal to:

$$\frac{False\ Positives + False\ Negatives}{|S\ \cup\ T|}$$

The Jaccard Distance is defined for binary masks, which makes it ideal for the one-vs-many masks that GlauNet uses (Kayalibay 2017).

The loss function which is chosen for a neural network must be differentiable if a neural network is to train, and the Jaccard Distance is differentiable. Moreover, for the purposes of the current image segmentation problem, the Jaccard Distance will "reflect both size and localization agreement" (Bertels 2019), which is necessary to correctly determine the location of the cup and disc. Additionally, per Bertels, Jaccard loss has "the most impact for refining the segmentations of samples of small size," which is important for medical image segmentation, as medical image corpuses tend to be relatively small.

Once it is calculated, the loss function must be used to optimize the network, which will minimize the loss and in principle make the network's learned model more correct. The stochastic gradient descent (SGD) optimizer is the most popular but it functions properly only when the learning rate of the network scales inversely with respect to time. The Adam (adaptive moment estimation) optimizer updates SGD by adapting the learning rate so it scales with the gradient of the loss (Rezaul 2018). Rezaul reports that Adam "performs well in most cases." Additionally, Adam allows for batch sizes - the number of images processed by the network before recalculating the network's weights - to be large or small. To keep the memory footprint of GlauNet minimal while it is learning, the network's batch size is 1.

4.7.2. Layer-Scale Hyperparameters

There are three basic hyperparameters for a single convolutional layer: the size of the kernel, the stride the kernel moves by, and the number of kernels used (Wei 2019). Rather than

being found via a search, these hyperparameters were set after considering the needs of the network.

The kernel used in the network's convolutional layers was the smallest useful kernel possible: three by three pixels. Smaller kernels were used because larger kernels will "reduce localization accuracy," according to Ronneberger et al, and the problem at hand requires carefully localizing any discovered features because we must find very precise edges to the cup and disc to allow for accurate measurement of the cup-to-disc ratio. Wei et al point out that smaller kernels allow for more complexity in a network's model than do larger kernels, and smaller kernels also decrease the number of parameters which decreases the time required to train a network (Wei 2019).

The stride of the network - the pixel distance a kernel is moved with each step - is one, as small as possible, so that no detail is missed and no context between features is lost, at the cost of the network training more slowly. Using a small kernel, which captures even small details, and moving that kernel as little as possible between iterations, will allow the network to capture details of the image while still eventually encompassing the entire image.

The number of kernels in each convolutional layer increases by a factor of two with each level deeper in the network. This is recommended by a number of authors (e.g. Milletari 2016, Iglovikov 2018, Chen 2018). The initial number of kernels in the shallowest layers was set at 64, with deeper layers containing 128, 256, 512, and 1024 kernels respectively. These quantities were chosen because they were large enough to capture significant numbers of features, while being small enough to fit within a reasonable amount of memory.

One layer-scale hyperparameter could not be chosen based on logic or previous experience: the initial learning rate given to the Adam optimizer, which affects the rate at which weights are updated during training. Choosing an incorrect learning rate can cause a network to become trapped in a local minimum, rather than finding the global optimum (Leondes 1998). To find a workable learning rate, a fast (and therefore numerically larger) learning rate was initially chosen, as if it were near the correct value, a faster learning rate would likely find its global optimum more quickly than would a slower learning rate. A learning rate of 0.01 was chosen as the starting point. This failed entirely to learn, resulting after several epochs in a network which was predicting all pixels to be of a single class instead of segmenting the image, making it

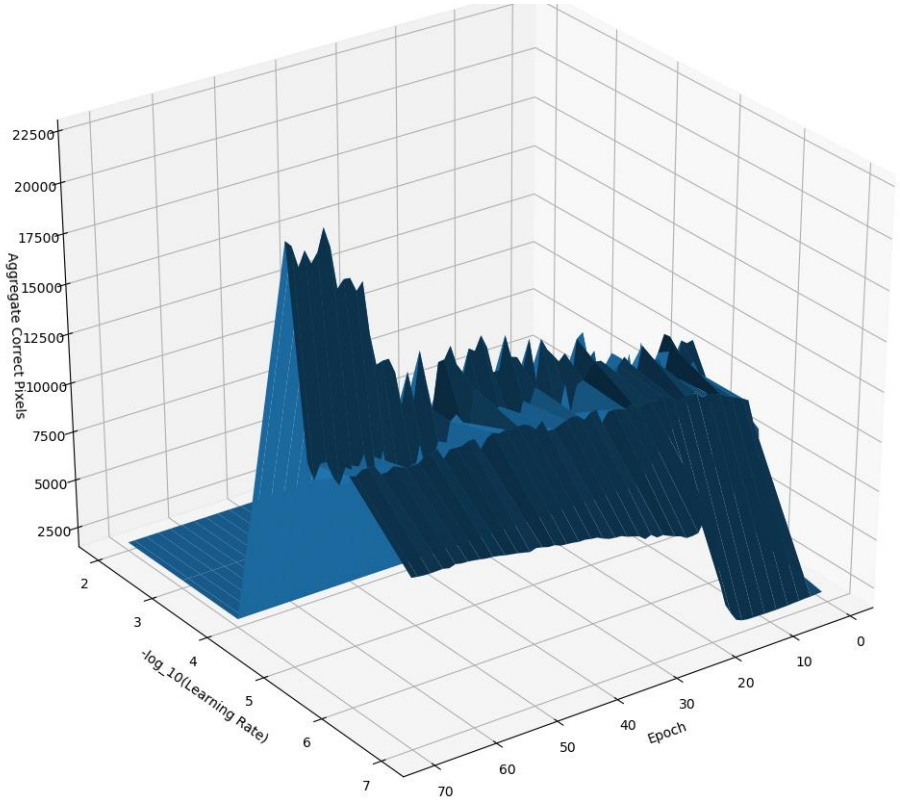

Figure 17: Graph of Aggregate Correctness by $-\log_{10}$(Learning Rate) and Epoch, to 70 Epochs

entirely useless. The learning rate was iteratively decreased by a factor of 10, and retrained. As the learning rate was decreased from 0.01 to 0.001, to 10^{-4}, the network continued to converge into a state which predicted only one class for all pixels. At 10^{-5}, however, the network converged to a correct prediction.

A second set of test runs was then undertaken; the learning rate of 10^{-5} was increased and decreased by a factor of 5, to $5x10^{-5}$ and $5x10^{-6}$, and these new networks were trained to a minimum of 250 epochs using each learning rate, but this caused the network to again converge to less correct models than did the 10^{-5} network.

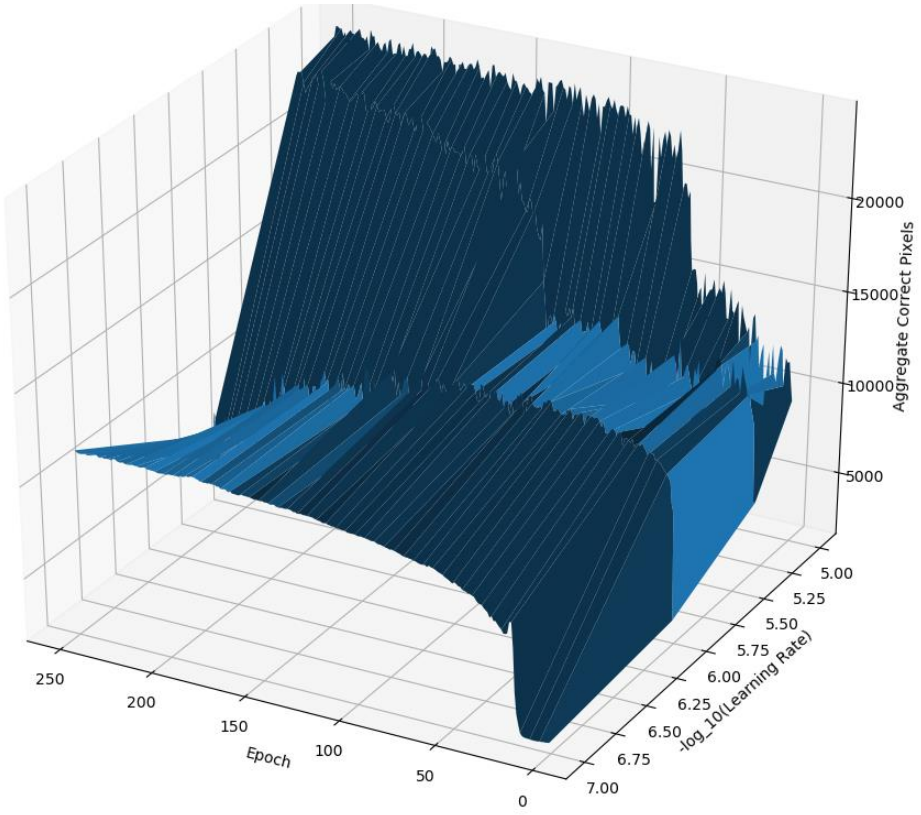

Figure 18: Graph of Aggregate Correctness by $-\log_{10}$(Learning Rate) and Epoch, to 250 Epochs

The graphs Figures 17 and 18 show the networks learning (or failing to learn). The graphs show learning as aggregate correct pixels, which is the number of correct pixels minus the number of incorrect pixels; this is a measure of learning which is unfeasible for training a network, but which is human-understandable. The networks were trained using the Jaccard Distance, which is described above.

The hyperparameters discussed in this section are summarized in Table 5.

Hyperparameter	Value
Activation Function	ReLU
Initializer	He normal
Loss Function	Jaccard Distance
Optimizer	Adam
Optimizer Learning Rate	10^{-5}
Kernel Size	3x3
Kernel Stride	1
Number of Kernels	64 - 1024

Table 5: Hyperparameters

4.8. Software

Two major software packages were used in this project: TensorFlow/Keras, and Singularity.

Singularity[5] is a free and open software program which runs containers which contain virtualized Linux systems. The intention of Singularity is to provide reproducible environments, compatibility with diverse computational architectures, and the running of software by "untrusted users running untrusted containers." This means that a complete Linux environment can be packaged and ported to a system running Singularity, and that it can be run (and installed,

[5] The user documentation for Singularity, including installation instructions, is available at https://sylabs.io/docs/

depending on the security rules on the local system) without requiring root or administrator privileges.

TensorFlow[6] is a free and open library designed for differentiation, which is frequently used for machine learning tasks. TensorFlow underlies Keras,[7] which is a free and open source library specifically for building neural networks.

[6] TensorFlow has extensive documentation available at https://www.tensorflow.org/
[7] Documentation available at https://keras.io/

5. Results

5.1. Training

A human ophthalmologist separates a fundus image into three separate classes: optic cup, optic disc, and background. The neural network presented in the previous section was designed to recognize the optic disc, because the sets of pixels for the cup, disc, and background are disjoint. Therefore, determining the extent of the optic disc also determines the extent of the optic cup and the background. This is most easily seen using the idealized fundus image in Figure 19, in which the optic cup is depicted in red, the optic disc in black, and the background in blue.

Figure 19: Idealized region of interest in a fundus image

Blue: background, Black: optic disc, Red: optic cup

Note that, when calculating the areas of a segmentation, the optic disc is the red and black regions combined.

The trained networks therefore segment a fundus image into the optic disc and "other." This limits the scope of the problem, and makes training the networks faster without losing any information.

Six networks were trained from scratch, one for each human annotator in the RIGA dataset. Each network had the same base architecture, described in the previous sections, but due to the presence of dropout in the architecture causing randomized neurons to "drop out" of the network, the finalized architectures will differ on the scale of individual neuron connections.

The corpus of training data was split into two sets: roughly 80% training data, and 20% validation data. The image files contain a serial number which increments by one, so validation images were chosen by selecting the images whose file number is evenly divisible by five, which was done to apply an algorithm which gave repeatable numbers. The number of images in each set is shown in Table 6.

Model	Annotator	Num. of Training Images	Num. of Validation Images
A	1	127	29
B	2	102	26
C	3	130	32
D	4	106	24
E	5	114	30
F	6	111	29

Table 6: Number of Images per Training and Validation Set by Model

During training, the networks updated their weights against the training data, and then the validation images were run through the updated network to calculate the loss as a performance measure. The loss at the end of each epoch was captured, and compiled into graphs to visualize the learning curve of each model, shown in Figure 20.

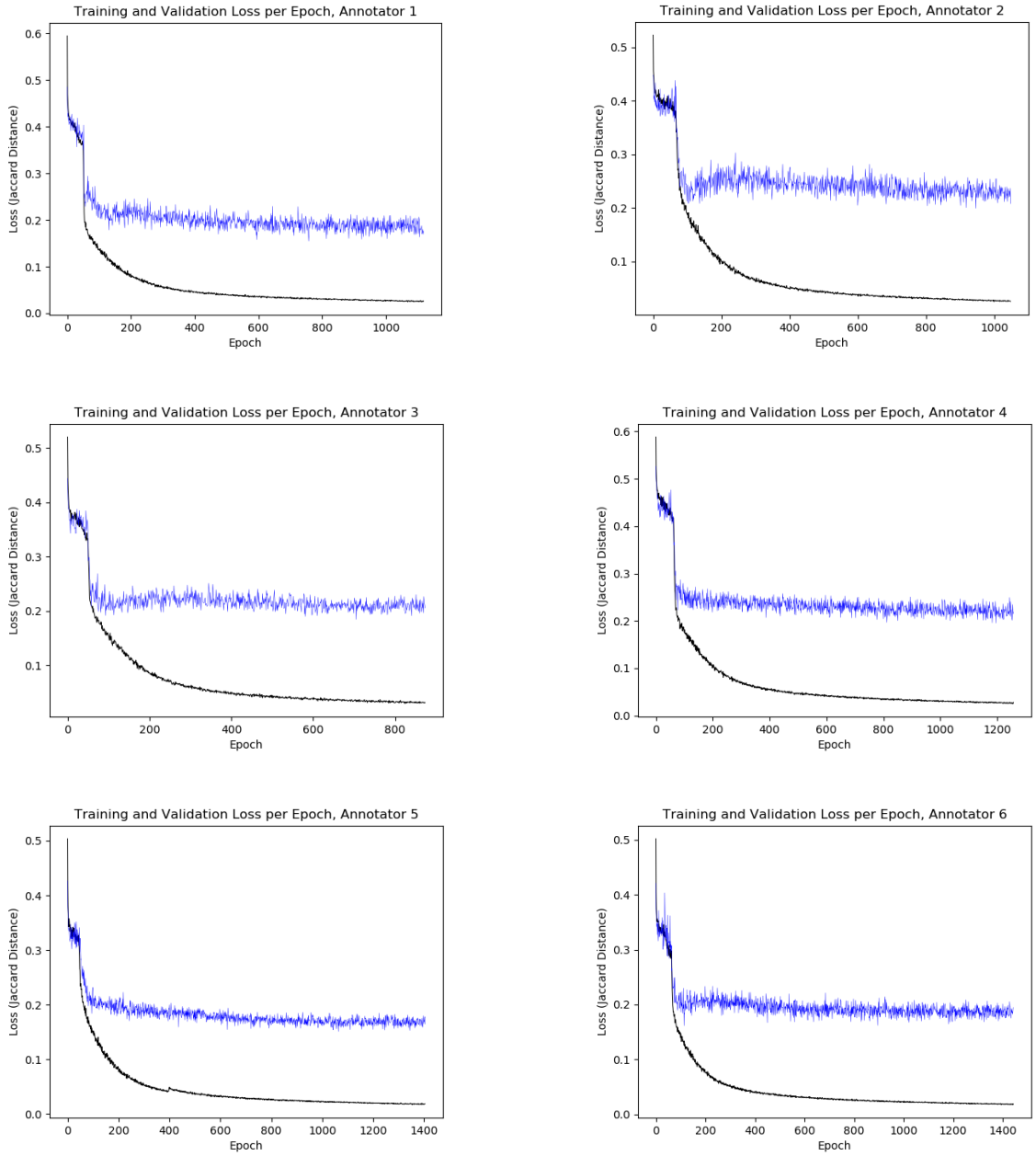

Figure 20: Training Performance of Each Model

Training loss in black, validation loss in blue.

It is immediately apparent that the loss drops significantly after approximately 50 epochs of training. The order of the training images was randomized before each training epoch was run, so the order in which the images were fed into the network during training did not cause this effect. The sharp drop in the loss is not an error or a flaw in the training; it is due to the network

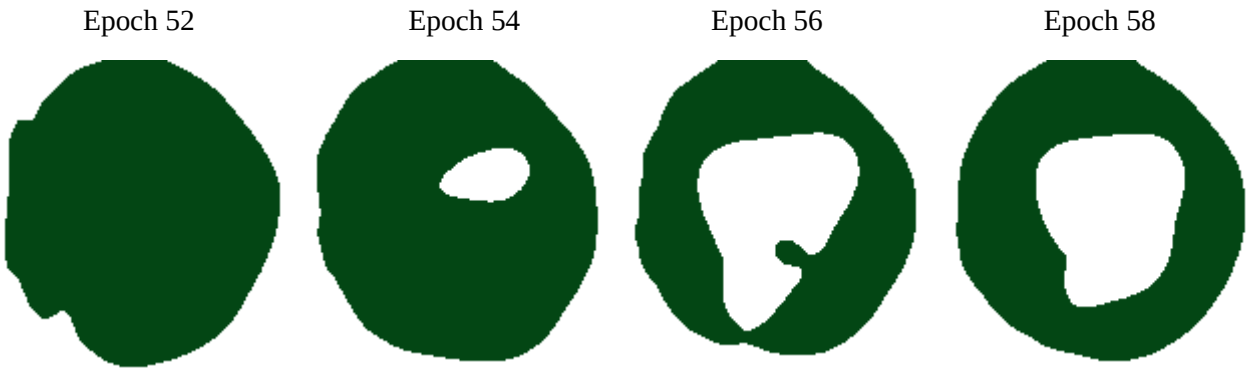

Figure 21: Optic Disc Predicted by Model C at Progressive States of Learning

encoding the existence of a hole in the center of the annotation where the optic cup is found. A series of predictions, shown in Figure 21, was captured which shows this learning process for Model C, which is learning to predict Annotator 3. The ground truth for Annotator 3 which the model is attempting to predict is shown in Figure 22.

Figure 22: Ground Truth Optic Disc Annotation by Annotator 3

The network weights which produced the best loss were saved as an ongoing process, so the final network for each annotator is the one among all the networks trained which provides the best model for that annotator. When loaded into TensorFlow, each model will predict how an individual human annotator would have segmented a given fundus image. These six models were then tested to determine how correct their predictions were.

The training of a neural network is in general a stochastic procedure, so each time a network is trained *de novo* the resulting network will be different. This makes it difficult to

compare the six models on a micro-level, but they remain similar in their overall design, which was detailed in Section 4.

5.2. Correctness Metrics

After the models completed training, all the fundus images in the validation data for each annotator were processed through the system against each of the six annotators to determine how correct the system would be. The number of images tested per annotator is shown in Table 7. Python programs were written which loaded each annotator's model in turn and processed all validation files against that annotator. The training data was not used, as it would be more likely to be correctly segmented by the network and therefore would bias the calculations towards finding that the predictions are correct.

Network	Annotator	Num. of Images Tested
A	1	29
B	2	29
C	3	30
D	4	24
E	5	30
F	6	29

Table 7: Number of images tested for correctness

5.2.1. Pixelwise Percent Incorrect, Precision, Recall, and F Measure

Note that the area of the disc includes the cup (Almazroa 2016, Almazroa 2017), and in fact the cup is often called the "cup of the optic disc" (Chakravarty 2017). This is illustrated for an idealized fundus image in Figure 23. This is important to keep in mind when discussing the correctness of the segmentation of the disc.

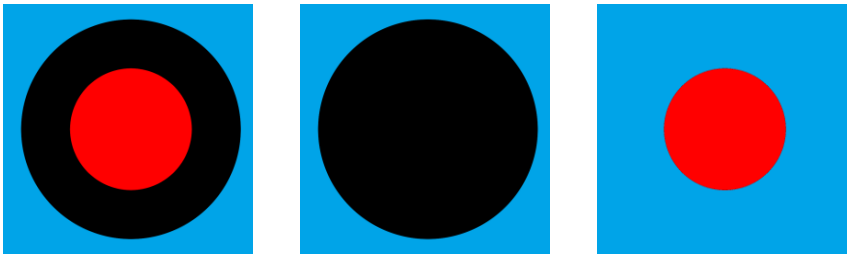

Disc and cup Area of disc Area of cup

Figure 23: Cup and disc delineated on an idealized fundus image

Blue: background; Black: disc; Red: cup

The number of pixels which each prediction correctly or incorrectly identified were counted, and an image was created for each prediction showing where the ground truth and the predicted segmentation differed. Evaluation metrics were calculated using the predictions and the ground truth data, which is tabulated in Table 8. The F-Measure is the harmonic mean of precision and recall.

Model	Annotator	Percent Incorrect	Mean Precision	Median Precision	Mean Recall	Median Recall	Mean F measure	Median F Measure
A	1	9.6%	0.8790	0.8924	0.9080	0.9206	0.8909	0.9043
B	2	11.3%	0.8646	0.8879	0.8800	0.9020	0.8683	0.8688
C	3	11.1%	0.8648	0.8826	0.9038	0.9093	0.8816	0.8957
D	4	10.3%	0.8547	0.8613	0.8987	0.9165	0.8738	0.8822
E	5	9.4%	0.9080	0.9135	0.9096	0.9239	0.9068	0.9104
F	6	10.2%	0.8846	0.9123	0.9055	0.9114	0.8923	0.9045
All	All	10.3%	0.8768	0.8904	0.9015	0.9138	0.8863	0.8974

Table 8: Pixelwise Evaluation Metrics by Model

The pixelwise percent incorrect measure was calculated as follows:

percent incorrect = (false positives + false negatives) / total pixels

For all annotators, the predicted images were incorrect, in the mean, by 10.3%. The individual annotators varied slightly from this average. Note that Model D, based on Annotator

4, predicts 10.3% incorrect pixels, which is also the mean incorrectness among all predictions by all the models. This is interesting because Almazroa, et al, report that Annotator 4 "had the best agreement with all other ophthalmologists in terms of disc area and centroid markings," which "means that [he or she] provided good disc boundary markings" (Almazroa 2016). Since Model D's predictions are in the middle of the pack, so to speak, it appears to agree in general terms with the other five models in much the same way Annotator 4's markings agreed best with their fellow ophthalmologists'. However, the precision, recall, and F measure for Model D are lower than the equivalent metrics for all models except for median recall. This implies that Model D is actually worse at predicting its annotations than average for all models.

To give a baseline, masks which "predicted" all pixels as belonging to the optic disc class or the non-optic disc class were created, and compared to the validation data for each annotator. The information is summed up in Table 9.

Model	Annotator	Percent Incorrect if Predict All Class 0	Percent Incorrect if Predict All Class 1
A	1	44.2%	55.8%
B	2	43.1%	56.9%
C	3	48.2%	51.8%
D	4	41.4%	58.6%
E	5	50.3%	49.7%
F	6	48.2%	51.8%
All	All	46.2%	53.8%

Table 9: Percentage of Pixels Predicted Incorrectly for Single-Class Predictions of Class 0 (Baseline) or Class 1 (Optic Disc)

The models' predictions in general captured the shape of the ground truth annotations, as can be seen in Figure 24. Each of the annotators has a distinctive signature to his or her segmentations of the image which can be seen by a human observer. For example, annotators 1 and 2 tend to segment the optic disc – the "hole" in the center of the segment – with a larger area than do annotators 5 and 6. This behavior is captured by the models, albeit imperfectly. These imperfections are caused, for instance, by the organic shapes of the blood vessels in the fundus image that could confuse the model, which can

be seen especially well in Models A, B, and F, for the predicted disc, for this test instance. Note, for example, the high rate of correctness for Model F in Figure 24, below. These metrics are good, even though the model has made a serious error in segmenting the optic cup. The model appears to have been confused by the blood vessel in the lower quadrant of the optic disc. However, this error is small in area, so it doesn't change the pixelwise precision or recall by a large amount. It does, however, make the C/D ratio significantly incorrect.

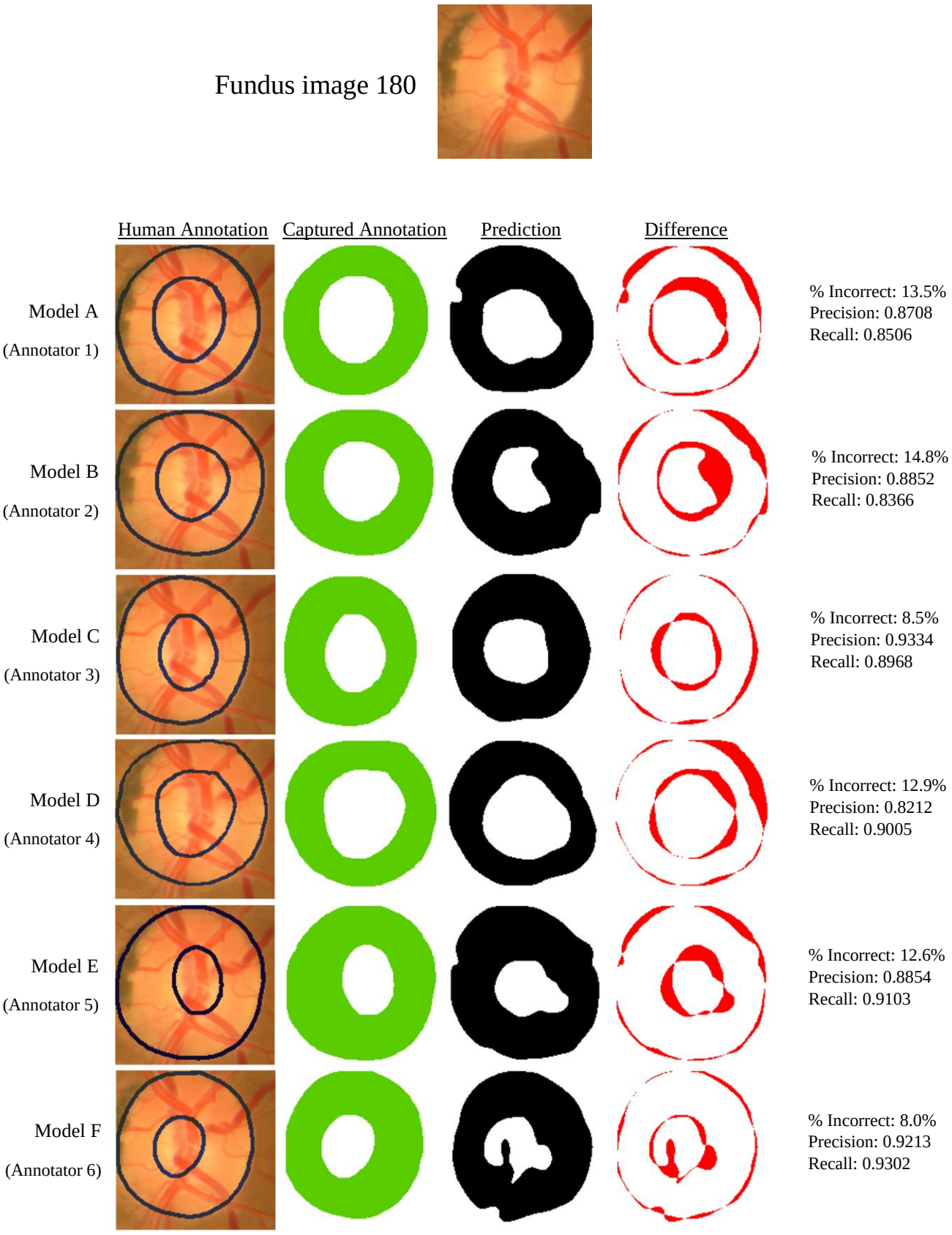

Figure 24: Annotations, Predictions, Ground Truth, and Differences

5.2.2. Pixelwise Dice Similarity

Per Thada and Jaglan (Thada 2013), the Dice similarity coefficient for sets X and Y is given by:

$$\text{Dice}(X,Y) = 2\,\frac{|X \cap Y|}{|X|+|Y|}$$

A program was written in Python to measure the Dice similarity coefficient was measured for predictions made by each model in GlauNet against the validation set. The results are summarized in Table 10. A higher Dice coefficient represents a better prediction by the network. The Dice similarity coefficient is similar to the Jaccard metrics described in the next subsection; however, unlike the Jaccard Distance, (1 – Dice) does not obey the triangle inequality. The triangle inequality – the requirement that

$$\text{dist}(x,z) \leq \text{dist}(x,y) + \text{dist}(y,z)$$

– is one of the properties required for a proper distance metric (Ontañón 2020).

Model	Annotator	Dice coefficient	
		Mean	Median
A	1	0.891	0.904
B	2	0.868	0.869
C	3	0.882	0.896
D	4	0.874	0.882
E	5	0.907	0.910
F	6	0.892	0.904
All	All	0.886	0.897

Table 10: Mean and median pixelwise Dice similarity coefficients for GlauNet models

5.2.3. Pixelwise Jaccard Metrics

Using a Python program, the Jaccard Index and Jaccard Distance[8] were measured for GlauNet's predictions. The results are summarized in Table 11.

The Jaccard Distance was used as the loss function when training the neural networks. A higher Jaccard Index (or a lower Jaccard Distance) indicates that two sets are more congruent, and therefore in the case of a neural network, that the prediction is closer to the ground truth.

Model	Annotator	Disc		Cup	
		Mean	Median	Mean	Median
A	1	91.20	91.96	81.26	83.84
B	2	89.04	89.79	74.59	76.98
C	3	90.43	92.13	72.34	76.27
D	4	91.05	92.15	81.09	82.88
E	5	91.40	91.62	75.55	78.15
F	6	90.34	90.66	71.43	70.75
All	All	90.59	91.40	75.85	78.20

Table 11: Mean and median pixelwise Jaccard Index percentages for GlauNet's models

5.2.4. C/D Ratio Percent Incorrect, Precision, Recall, and F Measure

The range of C/D ratio values which define an eye as glaucomatous or non-glaucomatous are: less than 0.4 is likely non-glaucomatous, 0.4 to 0.8 can be suspect for early glaucoma, and greater than 0.8 should be "consider[ed] glaucomatous unless proven otherwise" (Tsai 2005). Positive and negative predictions, then, are defined in terms of predictions matching or failing to match the diagnosis for a given annotator. This leads to definitions of true and false negative, and true and false positive, which are given in Table 12.

[8] The Jaccard Index and Distance are explained in Section 4.7.1. Briefly, the Jaccard Index measures the difference between two sets, and the Jaccard Distance is 1 – (Jaccard Index), used as a loss function.

model / human	CDR < 0.4	0.4 ≤ CDR ≤ 0.8	CDR > 0.8
CDR < 0.4	True Negative	False Positive	False Positive
0.4 ≤ CDR ≤ 0.8	False Negative	True Positive	False Positive
CDR > 0.8	False Negative	False Negative	True Positive

Table 12: Definitions of TP, TN, FP, and FN for C/D ratio

A C/D ratio was calculated for each annotator's segmentation of the fundus image. Then this C/D ratio was compared to a C/D ratio calculated using the segmentation predicted by the model trained on that annotator's work. Precision, recall, and the F-measure were calculated using the definitions of true/false positives and negatives given in Table 11. The percentage incorrectness was calculated using the metric which would capture any incorrectness on the part of the models: to be counted as correct, the model was required to exactly match the diagnosis based on the human's annotations; e.g., to be counted as correct when the human diagnosis would be "suspect for early glaucoma," the model must predict a C/D ratio between 0.4 and 0.8. The results of these calculations are summarized in Table 13.

Model	Annotator	Percent Incorrect	Precision	Recall	F-Measure
A	1	0.0	1.000	1.000	1.000
B	2	11.5	0.920	0.958	0.939
C	3	21.9	0.885	0.852	0.868
D	4	0.0	1.000	1.000	1.000
E	5	20.0	0.826	0.905	0.867
F	6	21.4	0.875	0.875	0.875
All	All	13.0	0.920	0.946	0.933

Table 13: Precision, recall, and F-measure for the cup-to-disc ratio by annotator

There is noticeable variation in the correctness metrics. Models C, E, and F, which are all 20% or more incorrect and below 0.9 in precision, recall, and F-measure, do remarkably

worse than models A and D, which properly predicted all the instances put to them. It is not clear why this is, but note the number of epochs of training for each model, in Table 14.

Model	Annotator	Number of Epochs Spent in Training
A	1	1118
B	2	1049
C	3	874
D	4	1258
E	5	1404
F	6	1444

Table 14: Number of epochs of training per model

Model C trained for notably fewer epochs than did models A and D, while models E and F trained for notably more epochs than did A and D.[9] So perhaps model C is underfitting while models E and F are overfitting, but more research would be necessary to determine the exact cause of the difference in the accuracies of the models.

Models C, E, and F do not show this same significant difference in metrics on the pixelwise measures of accuracy. This is because the pixelwise measures are considering the predicted and the ground truth segmentations as sets, whereas the C/D ratio is based entirely on the shape of the segmentation. Small changes in the shape of the segmentation can have a very small effect on the pixelwise measures, but can have a very large effect on a measure of accuracy which is specifically measuring shape.

[9] An epoch is a single session of training against all images in the training set, in randomized order.

6. Ease and Economy of Use

6.1. Containerization via Singularity

GlauNet is intended for use by persons with minimal computer experience. However, the neural network system used by GlauNet, TensorFlow, can be difficult to install and can be confusing to use, especially when more than one model is being utilized. Therefore, it would be valuable to have a drop-in appliance which would remove any need for the user to interact with TensorFlow. Fortunately, this can be done using Singularity, which containerizes an entire Linux install and its installed packages into a single image file.

Virtualized Linux systems can run in Singularity containers. This provides reproducible environments, the ability to run desired software on many different computational architectures, and allows untrusted users to run untrusted containers. A complete Linux environment can be packaged and ported to a system that has Singularity installed. Singularity can be run (and, if the security rules of the allow it, can be installed) without requiring a user to have root or administrator access. One of the use cases for Singularity is as a create-and-deploy solution for complex software installs, also called a software appliance, which GlauNet is intended to be (Kurtzer 2017)

The GlauNet image file can be loaded by Singularity to instantiate a container which can be used to run Linux and its installed programs. The user therefore only needs to install Singularity using a single apt command, upload the Singularity image file for this project and a few auxiliary files, and thereafter can use GlauNet without significant knowledge of Linux or any knowledge of TensorFlow, Python, or any of the other tools used to create this project.

A Singularity 2.4.2 image was created which contained Ubuntu Linux 18.04, a full installation of TensorFlow and libraries such as Pillow, used to process images, and NumPy, used to handle arrays. The container was set up to allow input from the host system running

Singularity, and output to the host system's hard drive. This allows for data to be saved permanently; the data inside a Singularity container are by default immutable and will be the same each time the container is instantiated. The Singularity container was given a runscript, which means that when it is instantiated it will immediately run a program without any input from the user. This limits the amount of knowledge that the user must have, as it limits the number of steps he or she must take to use the system.

This runscript is a Python program which loads the TensorFlow libraries and then processes each of the fundus images in a specific directory, inputting each image into each of the six annotator models in sequence. The resulting predicted segmentation is then processed to capture the horizontal size of both the cup and disc, and a cup/disc ratio is calculated. Then the name of the fundus image file, the cup size, the disc size, and the cup/disc ratio are written to a file on the host machine. This file compiles the information for all the images in once place for ease of use.

The runscript processes all tiff images in the `/incoming` directory, uses the models placed in the `/worksite` directory, and reports the cup/disc ratios to the `/outgoing` directory.

This is still not simple enough, though. A Singularity instance can be complicated to call from the command line, especially when the image must read data from and write data to the host system. Therefore, to make using the Singularity image as simple as possible a user script

was created which automates the process. To install the image, a user will drop the Singularity image and the user script anywhere on the host system, and then place the model files and one Python program in the `/worksite` directory. Having one Python program and the six model files external to the Singularity image allows for simple upgrades if updated images or a new loss function are created.

To predict the cup/disc ratio the user need only place one or more tiff-formatted fundus images in the `/incoming` directory and call the user script. The systems within the image will read in the images, process them, and output the cup/disc ratio to a file on the host system. The Singularity instance is then unloaded from memory. The cup/disc ratio is reported as a single number, and the user does not need to do any calculations or understand the ophthalmological methods necessary to determine the extent of the cup and the disc.

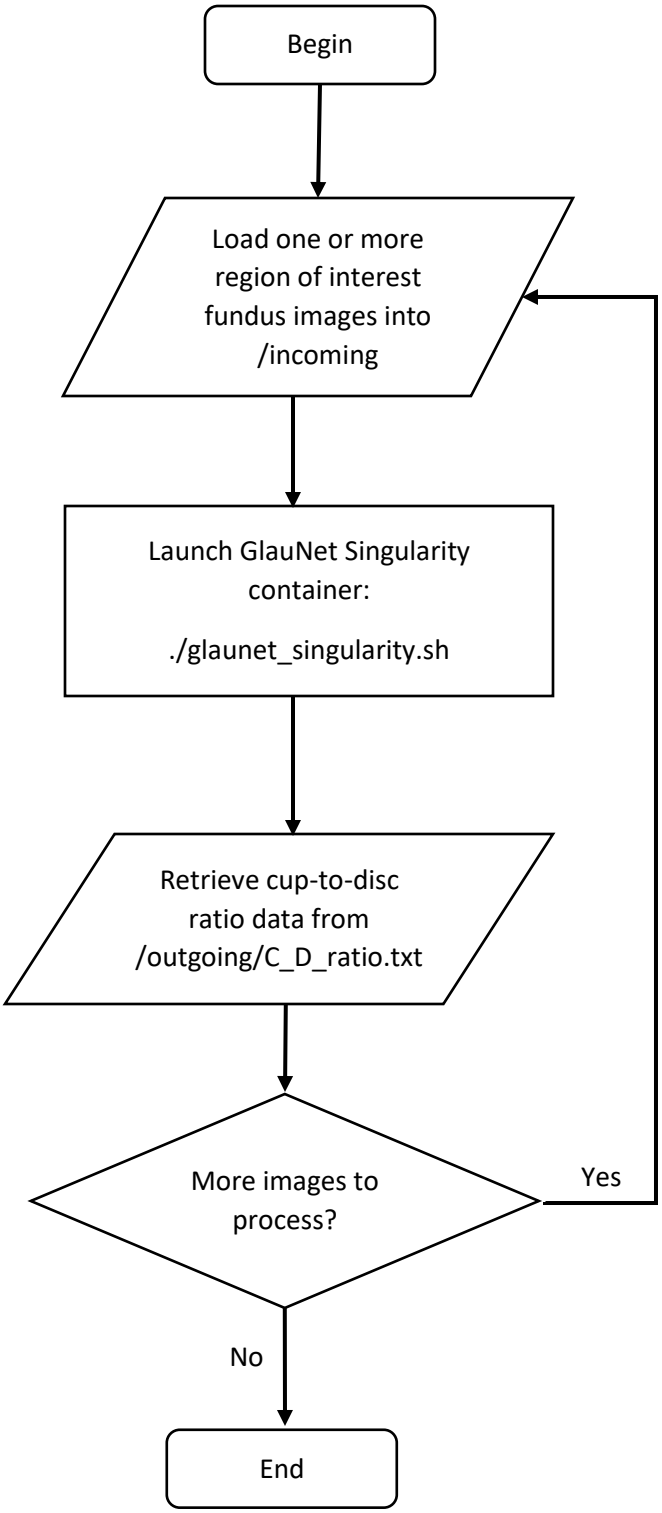

Figure 25: Flowchart of GlauNet usage

6.2. Feasibility of Inexpensive Hardware

The intent of the GlauNet system is to allow users without training as ophthalmologists to gain one piece of information that points to the likelihood of glaucoma. However, locations without access to ophthalmologists are likely to also have less access to powerful computers.

The training detailed above in this section created six separate models, each of which was packaged in a 355 MB H5 file. Files in the H5 format are designed to contain scientific data in a uniform, readable format, and TensorFlow reads H5 files natively. These H5 files are intended for distribution with GlauNet, and require no user intervention or understanding; they can be entirely black boxes to the end user.

To determine the feasibility of running the packaged Singularity image on inexpensive hardware, an experiment was performed on a CloudLab instance.[10] CloudLab is a "facility for building clouds." The CloudLab system gives access to bare-metal computers, and gives the user control over the networking and storage assets a cloud computer has access to. The system allows control of hardware down to the number of processors and amount of RAM per processor, allowing an experiment to be both repeatable and precise (CloudLab Team 2020).

A CloudLab instance containing one core from a single Intel Xeon Silver 4114 processor at 2.20 GHz was instantiated with 4 Gb of RAM. Ubuntu Linux 18.04 and Singularity version 2.4.2 were installed onto the instance. Detailed specifications of the instance hardware and software are given in Table 15.

Operating System	Ubuntu Linux 18.04
Containerization	Singularity 2.4.2
CPU speed	2,194.910 MHz
CPU cores	1
Cache size	14,080 KB
BOGOMIPS	4,389.82
Memory	4,089 MB
Storage	16,383 MB

Table 15: Test Machine Specifications

[10] The online interface to CloudLab is available at https://www.cloudlab.us

The six models and the 160x160 pixel region of interest fundus images for all annotators were uploaded to the instance using SFTP.

A wrapper script was written for the user script (see Section 5.3, above). The wrapper script outputs a timestamp before and after the user script is run, so it would be possible to determine how long the CloudLab instance spent loading Singularity, processing the fundus images through each of the six annotator models, and unloading Singularity. The wrapper script itself contained nothing between the two timestamp calls other than a call to the user script, and therefore added negligible time to the process.

Batches of one, two, four, eight, sixteen, and thirty-two images were processed through the system. The images were chosen by randomly selecting their file numbers without replacement using a pseudorandom number generator. Each fundus image was used as the input to each of the six models, in turn. Each of the three test runs for each image count used the same two, four, etc. images, to minimize experimental variables.

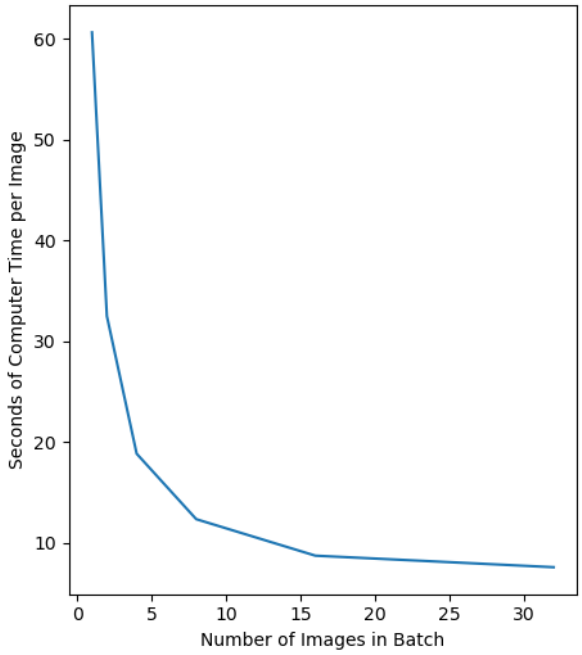

Figure 26: Mean Time to Process One Image in a Multi-Image Batch

In an attempt to minimize the effect of a random background process using CPU time and thereby increasing the time the Singularity container took to do its work, each image count was processed three separate times, and no user-initiated processes were running on the CloudLab

instance other than the wrapper script. The mean of the time required to process a single image across all three runs was calculated, and is graphed in Figure 26. The curve of the graph decays exponentially towards approximately seven seconds per image. When processing large batches, each additional file will take about this much time.

Separately, the time needed to load Singularity, to load the TensorFlow libraries within Singularity, and then to unload Singularity, was timed by running the wrapper script with no files for GlauNet to process. Across three such runs, the mean load-and-unload time was two seconds. It is clear, therefore, that the processor time required to run Singularity contributes negligibly to the time required to process an image. The only other time-consuming functions in the process of predicting a segmentation are loading the six models into TensorFlow, and the processing of the images themselves. Since we have demonstrated that each file takes only a few seconds to process, the majority of the time is spent in loading the models. This is not unexpected, as each model is 355 MB in size.

These tests were performed on a single 2.2 GHz CPU core. Processors of this speed were first released over a decade ago. The tests were also performed on a system with 4 GB of RAM, which is insufficient to run most modern operating systems other than Linux. This suboptimal machine was, however, able to process images and provide predictions for all six annotators in a very short time. When processing a single image, which would show the greatest effect from loading the models into TensorFlow, this test demonstrates that the user would still receive C/D ratio predictions for all six annotators in just over a minute.

7. Conclusion and Further Work

The system described in this thesis, GlauNet, provides a solution for using machine learning to automatically segment the optic disc and cup from region of interest fundus images, capture the cup-to-disc ratio from the segmentation, and output six calculated C/D ratios - one for each of the six annotators in the RIGA dataset. The mean error of GlauNet's predictions of pixel labels is 10.3% across all six of the models provided, with a mean precision of 87.7% and a mean recall of 90.1%. Its pixelwise mean Jaccard Distance from ground truth across all models is 20.2%.[11] The precision of the predicted cup-to-disc ratio across all six models is 0.920, the recall across all models is 0.946, and the F-measure across all models is 0.933.

For each of the six annotators whose work makes up the RIGA corpus, GlauNet captures a separate model and outputs a predicted cup-to-disc ratio for that annotator. This separation of the annotators appears to be unique, even though there is significant interannotator disagreement as to the segmentation of each fundus image. Other researchers who worked with the RIGA set have used techniques which either take all annotators together into a single model (Almazroa *IJBI* 2018), or combined the annotators' segmentations together into consensus annotations (Yu 2019).

More work can be done with this system. For instance, a method for importing a fundus image from a fundus camera would need to be implemented to make GlauNet a turnkey software appliance. Without access to a fundus camera, this is currently out of reach.

Some further work requires design and coding rather than access to hardware, For example, while the C/D ratio is a good metric for the development of glaucoma, there are more metrics which can be captured using a segmentation of the optic cup and disc. GlauNet captures

[11] A lower Jaccard Distance is better. 0% Jaccard Distance exactly replicates the ground truth.

the horizontal C/D ratio because "studies have shown that the vertical ratio increases faster in early and intermediate stages of glaucoma," allowing the disease to be detected earlier in its progress and heading off blindness with treatment (Tsai 2003). Changes in the morphology of the retina due to glaucoma can include the vertical C/D ratio being larger than the horizontal C/D ratio, adding another metric to the detection of the disease (Martus 2005). Specifically, an oval cup in a round disc can be indicative of glaucoma (Tomlinson 1974). The vertical C/D ratio can be captured from GlauNet's segmentations, which will allow the calculation of this new metric.

Notching and irregularities in the rim of the optic disc can be indicative of glaucoma (Danesh-Meyer 2006, Tsai 2003). A proper segmentation of the optic disc could detect such irregularities; however, GlauNet does not perfectly convey the border between the optic disc and the background of the fundus, making it difficult to find such irregularities. More work would need to be done, to make the models more precise, before such a metric could be captured from the segmentations.

Taking the opposite tack from identifying irregularities in the border of the segmentation, it is possible to improve a neural network's segmentation performance through postprocessing to reduce the irregularities in region boundaries, fill interior holes, and separate out clusters of labels with "weak connectivity" (Haidekker 2011). This process might hold some hope for improvement in the network laid out in this thesis, but the expert annotations which are the ground truth for this project contain intentional border irregularities, and the "hole" in the center of each segmentation is a vital piece of information for separating the optic disc from the optic cup.

Perhaps the most important improvement to the network provided in this thesis would be to automate the process of localizing the image to a region of interest. The region of interest in a

fundus image is the section surrounding the optic disc. For this project, the region of interest was localized using the human annotators' segmentations of the image. Almazroa and Burman have proposed a method of localizing the optic disc by finding the brightest spot in the fundus image, and centering the localized image there (Almazroa 2017). This localized image could then be either used as-is, or shown to a human as a sanity check, before being fed into the models to predict the segmentation of the image.

As the U-Net neural network architecture was used to implement the models, the memory footprint of the running network is minimized so that it can fit into less than 4 GB of memory with sufficient space for Linux and Singularity to run comfortably. This minimal footprint is necessary to fulfill the intentions of the project: a system which can run without issues on inexpensive hardware and software. The Singularity image is a 1.9 GB file, and therefore has not been uploaded to a publicly available location. It is, however, available upon request.

Works Cited

Almazroa A, S. Alodhayb, E. Osman, et al. “Agreement among ophthalmologists in marking the optic disc and optic cup in fundus images.” *International Ophthalmology: The International Journal of Clinical Ophthalmology and Visual Sciences*. 2016;37(3):701. doi:10.1007/s10792-016-0329-x.

Almazroa A, W. Sun, S. Alodhayb, K. Raahemifar, V. Lakshminarayanan. “Optic disc segmentation for glaucoma screening system using fundus images.” *Clin Ophthalmol*. 2017;11:2017-2029 https://doi.org/10.2147/OPTH.S140061

Almazroa A, W. Sun, S. Alodhayb, K. Raahemifar, V. Lakshminarayanan. “An Automatic Image Processing System for Glaucoma Screening.” *International Journal of Biomedical Imaging*. 2017;11:2017-2029 https://doi.org/10.1155/2017/4826385

Almazroa, Ahmed, Sami Alodhayb, Essameldin Osman, Eslam Ramadan, Mohammed Hummadi, Mohammed Dlaim, Muhannad Alkatee, Kaamran Raahemifar, Vasudevan Lakshminarayanan, “Retinal fundus images for glaucoma analysis: the RIGA dataset.” Proc. SPIE 10579, Medical Imaging 2018: Imaging Informatics for Healthcare, Research, and Applications, 105790B (6 March 2018); doi: 10.1117/12.2293584; https://doi.org/10.1117/12.2293584

Almazroa, A. (2018). “Retinal fundus images for glaucoma analysis: the RIGA dataset [Data set]”. University of Michigan - Deep Blue. https://doi.org/10.7302/Z23R0R29

Alto, Valentina. “Neural Networks: parameters, hyperparameters and optimization strategies.” *Towards Data Science*. July 5, 2019. https://towardsdatascience.com/neural-networks-parameters-hyperparameters-and-optimization-strategies-3f0842fac0a5

Amazon. “Amazon EC2 Pricing.” Web. 2020. https://aws.amazon.com/ec2/pricing/on-demand/

Aquino, Arturo, Manuel Emilio Gegúndez-Arias, and Diego Marín. "Detecting the optic disc boundary in digital fundus images using morphological, edge detection, and feature extraction techniques." *IEEE Transactions on Medical Imaging*. 2010; 29(10) 1860-1869

Armaly MF. Genetic Determination of Cup/Disc: Ratio of the Optic Nerve. *Arch Ophthalmol*. 1967;78(1):35–43. doi:10.1001/archopht.1967.00980030037007

Arnekvist, Isac, J. Frederico Carvalho, Danica Kragic, and Johannes A. Stork. 2020. "The Effect of Target Normalization and Momentum on Dying ReLU." https://search.ebscohost.com/login.aspx?direct=true&AuthType=sso&db=edsarx&AN=edsarx.2005.06195&site=eds-live&scope=site.

Bertels, Jeroen, Tom Eelbode, Maxim Berman, Dirk Vandermeulen, Frederik Maes, Raf Bisschops, and Matthew Blaschko. 2019. "Optimizing the Dice Score and Jaccard Index for Medical Image Segmentation: Theory & Practice." doi:10.1007/978-3-030-32245-8_11.

Blanford, Richard. "Beware the hidden costs of cloud computing." 2018. IT Pro Portal. https://www.itproportal.com/features/beware-the-hidden-costs-of-cloud-computing/

Buda, Mateusz, Atsuto Maki, and Maciej A Mazurowski. "A Systematic Study of the Class Imbalance Problem in Convolutional Neural Networks." *Neural Networks* 106 (2018): 249-59.

Budenz, Donald L, Keith Barton, Julia Whiteside-de Vos, Joyce Schiffman, Jagadeesh Bandi, Winifred Nolan, Leon Herndon, Hanna Kim, Graham Hay-Smith, and James M Tielsch. "Prevalence of Glaucoma in an Urban West African Population: The Tema Eye Survey." *JAMA Ophthalmology* 131.5 (2013): 651-58.

Chakravarty, Arunava, and Jayanthi Sivaswamy. 2017. “Joint Optic Disc and Cup Boundary Extraction from Monocular Fundus Images.” *Computer Methods & Programs in Biomedicine* 147 (August): 51–61. doi:10.1016/j.cmpb.2017.06.004.

CloudLab Team, The. “The CloudLab Manual.” 2020. http://docs.cloudlab.us/cloudlab-manual.html

Danesh-Meyer, H V, B J Gaskin, T. Jayusundera, M. Donaldson, and G D Gamble. “Comparison of Disc Damage Likelihood Scale, Cup to Disc Ratio, and Heidelberg Retina Tomograph in the Diagnosis of Glaucoma.” *British Journal of Ophthalmology* 90.4 (2006): 437-41.

Duplyakin, Dmitry, Robert Ricci, Aleksander Maricq, Gary Wong, Jonathon Duerig, Eric Eide, Leigh Stoller, Mike Hibler, David Johnson, Kirk Webb, Aditya Akella, Kuangching Wang, Glenn Ricart, Larry Landweber, Chip Elliott, Michael Zink, Emmanuel Cecchet, Snigdhaswin Kar, and Prabodh Mishra. 2019. “Design and Operation of Cloudlab.” *Proceedings of the USENIX Annual Technical Conference (ATC)*. pp 1-14.

Dwivedi, Priya “Understanding and Coding a ResNet in Keras.” 2019. Web. https://towardsdatascience.com/understanding-and-coding-a-resnet-in-keras-446d7ff84d33

Edward, Deepak P., and Thasarat S. Vajaranant. *Glaucoma*. Oxford: Oxford UP, 2013. Oxford American Ophthalmology Library.

Escobar, Angela. "How Much Does Telemedicine Software Cost?" KompareIt. 2020. Web. https://www.kompareit.com/business/medical-telemedicine-how-much-cost.html

Fanelli, James L. “Same Cup, Different Ratios.” *Review of Optometry* 150 (10): 90–93 (2013).

Forchheimer, De Moraes, Teng, Folgar, Tello, Ritch, and Liebmann. “Baseline Mean Deviation and Rates of Visual Field Change in Treated Glaucoma Patients.” *Eye* 25.5 (2011): 626-32.

Foster, Paul J, Ralf Buhrmann, Harry A Quigley, and Gordon J Johnson. “The Definition and Classification of Glaucoma in Prevalence Surveys.” *British Journal of Ophthalmology* 86.2 (2002): 238-23842.

Ganesh Babu, T.R., S. Shenbaga Devi, and Rengaraj Venkatesh. “Automatic Detection of Glaucoma Using Optical Coherence Tomography Image.” *Journal of Applied Sciences* 12 (20): 2128-2138, 2012.

Ganesh Babu, T R, S Shenbaga Devi, and R Venkatesh. 2015. “Optic Nerve Head Segmentation Using Fundus Images and Optical Coherence Tomography Images for Glaucoma Detection.” *Biomedical Papers of the Medical Faculty of the University Palacky, Olomouc, Czechoslovakia* 159 (4): 607–15. doi:10.5507/bp.2015.053.

Google. “Classification: ROC Curve and AUC.” (2020) Web. https://developers.google.com/machine-learning/crash-course/classification/roc-and-auc

Haidekker, Mark. *Advanced Biomedical Image Analysis.* 2011. John Wiley & Sons.

Hao, Zhixu. “Implementation of deep learning framework – Unet, using Keras.” 2018. Web. https://github.com/zhixuhao/unet

Hao, Ziqiang, Guangxu Wan, Victor Oluwaferanmi Adewuyi, and Weida Zhan. 2020. “Improved Faster R-CNN for Detecting Small Objects and Occluded Objects in Electron Microscope Imaging.” Acta Microscopica 29 (1): 542–51.

Hayamizu F, Yamazaki Y, Nakagami T, and Mizuki K. “Optic Disc Size and Progression of Visual Field Damage in Patients with Normal-tension Glaucoma.” *Clinical Ophthalmology* (2013): 807-13.

He, Kaiming, Xiangyu Zhang, Shaoqing Ren, and Jian Sun. “Delving Deep into Rectifiers: Surpassing Human-Level Performance on ImageNet Classification.” *2015 IEEE International Conference on Computer Vision (ICCV)*, January 2015, 1026.

Hsieh Jui-chien, and Hsu Meng-Wei. 2012. “A Cloud Computing Based 12-Lead ECG Telemedicine Service.” *BMC Medical Informatics and Decision Making* 12 (1): 77. doi:10.1186/1472-6947-12-77.

Owen Jones, Robert Maillardet, and Andrew Robinson. *Introduction to Scientific Programming and Simulation Using R, Second Edition*. CRC Press: Parkville, Australia; 2014.

Rezaul, Karim and Pradeep Pujari. *Practical Convolutional Neural Networks*. Packt Publishing; 2018.

Kayalibay, Baris, Grady Jensen, and Patrick van der Smagt. 2017. “CNN-Based Segmentation of Medical Imaging Data.” https://search.ebscohost.com/login.aspx?direct=true&AuthType=sso&db=edsarx&AN=edsarx.1701.03056&site=eds-live&scope=site.

Kessing, Svend Vedel., and John Thygesen. *Primary Angle-closure and Angle-closure Glaucoma*. Hague, Netherlands : Gilsum, NH: Kugler ; Pathway Book Service, 2007.

Khalil. T., M. U. Akram, H. Raja, A. Jameel and I. Basit, “Detection of Glaucoma Using Cup to Disc Ratio From Spectral Domain Optical Coherence Tomography Images,” *IEEE Access*, vol. 6, pp. 4560-4576, 2018, doi: 10.1109/ACCESS.2018.2791427.

Kolb, H. "Facts and Figures Concerning the Human Retina." National Center for Biotechnical Information at the U.S. National Library of Medicine. 2017. https://www.ncbi.nlm.nih.gov/books/NBK11556/

Kooner, Karanjit S., and Thom J. Zimmerman. *Clinical Pathways in Glaucoma*. New York: Thieme, 2001.

Kurtzer GM, V. Sochat, MW Bauer. 2017 "Singularity: Scientific containers for mobility of compute." *PLoS ONE* 12(5): e0177459. https://doi.org/10.1371/journal.pone.0177459

Li, F., Ranjay Krishna, Danfei Xu, and Amelie Byun. "CS231n: Convolutional Neural Networks for Visual Recognition." (2020) Stanford University. Web. http://cs231n.stanford.edu/

Liu, J., D. W. K. Wong, J. H. Lim, H. Li, N. M. Tan, and T. Y. Wong. 2009. "ARGALI: An Automatic Cup-to-Disc Ratio Measurement System for Glaucoma Detection and AnaLysIs Framework." *Proceedings of SPIE*, no. 1 (November): 72603K.

Lu, Lu, Yeonjong Shin, Yanhui Su, and George Em Karniadakis. 2019. "Dying ReLU and Initialization: Theory and Numerical Examples." https://search.ebscohost.com/login.aspx?direct=true&AuthType=sso&db=edsarx&AN=edsarx.1903.06733&site=eds-live&scope=site.

Martus, Peter, Andrea Stroux, Wido Budde, Christian Mardin, Matthias Korth, and Jost Jonas. "Predictive Factors for Progressive Optic Nerve Damage in Various Types of Chronic Open-angle Glaucoma." *American Journal of Ophthalmology* 139.6 (2005): 999-1009

Medici Technologies. "Pricing." 2020. Web. https://www.medici.md/doctors/pricing

Mishkin, Dmytro, and Jiri Matas. "All You Need Is a Good Init," 2016. *International Conference on Learning Representations*.

Moraru, Aurelian. 2017. “The New Telemedicine Business Model.” *Benchmarking Telemedicine: Improving Health Security in the Balkans. NATO Science for Peace and Security Series-D: Information and Communication Security: Volume 49*. IOS Press.

Riccardo Miotto, Matteo Danieletto, Jerome R. Scelza, Brian A. Kidd, and Joel T. Dudley. 2018. “Reflecting Health: Smart Mirrors for Personalized Medicine.” *Npj Digital Medicine* 1 (1): 1–7. doi:10.1038/s41746-018-0068-7.

Mohammadi, S-Farzad, Sara Mirhadi, Hadi Mehrjardi, Akbar Fotouhi, Sahar Vakili, Mercede Majdi, and Sasan Moghimi. “An Algorithm for Glaucoma Screening in Clinical Settings and Its Preliminary Performance Profile.” *Journal of Ophthalmic & Vision Research* 8.4 (2013): 314-20.

Nithya, R. and N. Venkateswaran. (2015). “Analysis of Segmentation Algorithms in Colour Fundus and OCT Images for Glaucoma Detection.” *Indian Journal of Science and Technology*, 8.

Okimoto S, K. Yamashita, T. Shibata, Y. Kiuchi. 2015. “Morphological Features and Important Parameters of Large Optic Discs for Diagnosing Glaucoma.” *PLoS ONE* 10(3): e0118920.doi:10.1371/journal.pone.0118920

Ontañón, Santiago. “An Overview of Distance and Similarity Functions for Structured Data.” *Artificial Intelligence Review: An International Science and Engineering Journal*, 2020, 1. doi:10.1007/s10462-020-09821-w.

Ronneberger, Olaf, Philipp Fischer, and Thomas Brox. 2015. “U-Net: Convolutional Networks for Biomedical Image Segmentation.” https://search.ebscohost.com/login.aspx?direct=true&AuthType=sso&db=edsarx&AN=edsarx.1505.04597&site=eds-live&scope=site.

Rumelhart, David E., Geoffrey E. Hinton, and Ronald J. Williams. 1986. “Learning Representations by Back-Propagating Errors.” *Nature* 323 (6088): 533–36.

Shringarpure, Suyash, Andrew Carroll, Francisco M De La Vega, and Carlos D Bustamante. 2015. “Inexpensive and Highly Reproducible Cloud-Based Variant Calling of 2,535 Human Genomes.” *PLoS ONE* 10 (6): e0129277. doi:10.1371/journal.pone.0129277.

Sommer, A., J M Tielsch, J. Katz, H A Quigley, J D Gottsch, J C Javitt, J F Martone, R M Royall, K A Witt, and S. Ezrine. “Racial Differences in the Cause-specific Prevalence of Blindness in East Baltimore.” *The New England Journal of Medicine* 325.20 (1991): 1412-1417.

Song, T., F. Meng, A. Rodriguez-Paton, P. Li, P. Zheng, and X. Wang. 2019. “U-Next: A Novel Convolution Neural Network With an Aggregation U-Net Architecture for Gallstone Segmentation in CT Images.” *IEEE Access* 7 (January): 166823–32. doi:10.1109/ACCESS.2019.2953934.

TensorFlow Team. “TensorFlow Core v2.2.0.” 2020. https://www.tensorflow.org/api_docs.

Thada, Vikas, and Vivek Jaglan. “Comparison of Jaccard, Dice, Cosine Similarity Coefficient to Find Best Fitness Value for Web Retrieved Documents Using Genetic Algorithm.” *International Journal of Innovations in Engineering and Technology* 2, no. 4 (2013): 202-205.

Tomlinson, Alan and Calbert Phillips. “Ovalness of the optic cup and disc in the normal eye.” *British Journal of Ophthalmology*. 1974. 10.1136/bjo.58.5.543.

Tsai, C. “How to Evaluate the Suspicious Optic Disc.” *Review of Ophthalmology*, MD, New York City, Jun. 2005

Tsai, James C and Max Forbes. *Medical Management of Glaucoma*. Professional Communication Inc, Oklahoma; 2003. 240 Pages ISBN 1-884735-80-0 Media Type:textbook.

Wang, Ya X., Xu, Liang, Lu, Wen, Liu, Feng J., Qu, Yuan Z., Wang, Jian, and Jonas, Jost B. "Parapapillary Atrophy in Patients with Intracranial Tumours." *Acta Ophthalmologica* 91.6 (2013): 521-25.

Wu, Menglin, Theodore Leng, Luis de Sisternes, Daniel L Rubin, and Qiang Chen. 2015. "Automated Segmentation of Optic Disc in SD-OCT Images and Cup-to-Disc Ratios Quantification by Patch Searching-Based Neural Canal Opening Detection." *Optics Express* 23 (24): 31216–29. doi:10.1364/OE.23.031216.

Yu, Shuang, Di Xiao, Shaun Frost, and Yogesan Kanagasingam. 2019. "Robust Optic Disc and Cup Segmentation with Deep Learning for Glaucoma Detection." *Computerized Medical Imaging and Graphics* 74 (June): 61–71. doi:10.1016/j.compmedimag.2019.02.005.

This project would not have been possible without the annotations provided in the RIGA dataset, which were created by the MESSIDOR program, and the Magrabi Eye Center and Bin Rushed Ophthalmic Center in Saudi Arabia.